Bayesian inference of binary black holes with inspiral-merger-ringdown waveforms using two eccentric parameters

Antoni Ramos-Buades[1,2] Alessandra Buonanno,[2,3] and Jonathan Gair[2]

[1]*Nikhef, Science Park 105, 1098 XG Amsterdam, The Netherlands*
[2]*Max Planck Institute for Gravitational Physics (Albert Einstein Institute),*
Am Mühlenberg 1, Potsdam, 14476, Germany
[3]*Department of Physics, University of Maryland, College Park, Maryland 20742, USA*

Orbital eccentricity is a crucial physical effect to unveil the origin of compact-object binaries detected by ground- and spaced-based gravitational-wave (GW) observatories. Here, we perform for the first time a Bayesian inference study of inspiral-merger-ringdown eccentric waveforms for binary black holes with nonprecessing spins using two (instead of one) eccentric parameters: eccentricity and relativistic anomaly. We employ for our study the multipolar effective-one-body (EOB) waveform model SEOBNRv4EHM, and use initial conditions such that the eccentric parameters are specified at an orbit-averaged frequency. We show that this new parametrization of the initial conditions leads to a more efficient sampling of the parameter space. We also assess the impact of the relativistic-anomaly parameter by performing mock-signal injections, and we show that neglecting such a parameter can lead to significant biases in several binary parameters. We validate our model with mock-signal injections based on numerical-relativity waveforms, and we demonstrate the ability of the model to accurately recover the injected parameters. Finally, using standard stochastic samplers employed by the LIGO-Virgo-KAGRA Collaboration, we analyze a set of real GW signals observed by the LIGO-Virgo detectors during the first and third runs. We do not find clear evidence of eccentricity in the signals analyzed, more specifically we measure $e_{\text{gw, 10 Hz}}^{\text{GW150914}} = 0.08_{-0.06}^{+0.09}$, $e_{\text{gw, 20 Hz}}^{\text{GW151226}} = 0.04_{-0.04}^{+0.05}$, and $e_{\text{gw,5.5 Hz}}^{\text{GW190521}} = 0.15_{-0.12}^{+0.12}$.

I. INTRODUCTION

In the second part of this decade, the LIGO, Virgo and KAGRA (LVK) ground-based detectors [1–8] will be reaching design sensitivity, promising several hundreds of detection per year of coalescing binary black holes. Most of these binaries are expected to be formed via isolated binary evolution [9–22,22], and circularize due to GW emission [23] by the time they enter the detector frequency band. Nonetheless, a small fraction of these binaries may have non-negligible orbital eccentricity in the frequency band of ground-based detectors, if they form through dynamical captures and interactions in dense stellar environments, such as globular clusters [24–44] or galactic nuclei [45–52]. Hence, measuring orbital eccentricity in the GW signal from merging binaries provides crucial information about the origin, evolution and the properties of the population of such binaries [53–59].

With upgrades of existing ground-based detectors (e.g., A^+ and Virgo$^+$ [60–62]), and future next-generation detectors on the earth, such as the Einstein Telescope and Cosmic Explorer [63–66], and in space, such as LISA and TianQin [67,68], the fraction of GW events with non-negligible orbital eccentricity is expected to significantly increase [69–72]. All these projections have motivated, in the last years, the development of waveform models that include the effect of orbital eccentricity. Those waveforms have been used to analyze GW signals observed by LIGO and Virgo [73–88]. Some of these studies have found evidence of eccentricity, for instance, for GW190521, where Ref. [76] showed evidence for a highly eccentric precessing-spin binary, Ref. [81] showed evidence for an eccentric nonprecessing binary, and Ref. [82] found evidence for a nonspinning dynamical capture merger. However, each of these studies comes with their own limitations. For example, Ref. [76] used a sparse grid of numerical relativity (NR) waveforms for inference, Ref. [81] applied reweighing techniques for inference [73] combined with an inspiral-merger-ringdown (IMR) model based on the effective-one-body (EOB) formalism [89–93],

`SEOBNRE` [94–96] with only one eccentricity parameter, although the impact of the latter in the eccentricity posterior might be limited [97]. While Ref. [82] restricted the study to nonspinning dynamical captures using the waveform model `TEOBResumS-Dali` [98,99].

In this paper, we perform a Bayesian inference study using the waveform model `SEOBNRv4EHM` [100,101], which describes eccentric effects using two eccentric parameters: the initial eccentricity and the relativistic anomaly. `SEOBNRv4EHM` is built upon the quasicircular `SEOBNRv4HM` model [102] for binary black holes (BBHs) with nonprecessing spins and includes eccentric corrections up to 2PN order [100] in the $(l, |m|) = (2, 2), (2, 1), (3, 3), (4, 4), (5, 5)$ multipoles. When restricting to the $(l, |m|) = (2, 2)$ modes, we refer to the model as `SEOBNRv4E`. We modify the initial conditions of the original version of the `SEOBNRv4EHM` model, which was presented in Ref. [101], so that now they are specified at an orbit-averaged orbital frequency instead of an instantaneous orbital frequency. We show that this new parametrization simplifies the stochastic sampling across parameter space. Furthermore, in order to increase the efficiency in evolving the dynamics, we combine reduced tolerances of the Runge-Kutta integrator during the inspiral with the optimized Hamiltonian and integrator from Refs. [103,104], and assess the impact of these modifications in the accuracy of the waveform model across parameter space. We find that for most of the parameter space the loss of accuracy is $< 1\%$ in unfaithfulness, indicating that the more efficient version of the `SEOBNRv4EHM` is still highly accurate for our purposes.

With the more efficient model, we use a highly parallelizable nested sampler PARALLEL BILBY [105] to assess first the impact of the different initial conditions, which available in the `SEOBNRv4EHM` model. We find that the initial conditions specified at an orbit-averaged frequency perform as accurately as the ones specified at an instantaneous orbital frequency, but with a more efficient sampling of the parameter space, which translates into shorter wall clock times for the parameter-estimation runs. Furthermore, we show, for the first time, the impact of the radial phase parameter (i.e., the relativistic anomaly), using an inspiral-merger-ringdown model and a full parameter-estimation code (see, e.g., Ref. [97] for a study of the argument of periapsis based on the overlaps).

We also validate the model `SEOBNRv4EHM` by performing zero-noise injections of public eccentric NR waveforms from the Simulating eXtreme Spacetimes (SXS) catalog [106,107]. In particular we select a set of three equal-mass, nonspinning eccentric simulations with initial eccentricities measured from the orbital frequency at first periastron passage of 0.07, 0.13 and 0.25, respectively. In order to compare the eccentricity from NR waveforms and the `SEOBNRv4EHM` model, we choose a common definition of eccentricity based on the GW signal, $e_{\rm gw}$, as introduced in

Ref. [108], and measure it from the waveform using the `gw_eccentricity` package [109]. We find that `SEOBNRv4EHM` is able to accurately recover the injected parameters of the NR signals for all the eccentricity values considered.

Finally, we analyze some GW events observed by the LVK collaboration with `SEOBNRv4EHM`. In particular, we analyze GW150914 [110], GW151226 [111] and GW190521 [112,113]. The choice is based on the fact that the first GW signal is still one of the loudest GW events so far, and has been found as a noneccentric binary by many studies in the literature [73,85,86,114]. On the other hand, GW151226 and GW190521 have been found to have signatures of eccentricity by some studies in the literature [76,79,81,82,86]. We measure the following values of eccentricity for these GW events, $e_{\rm gw,\ 10\ Hz}^{\rm GW150914} = 0.08_{-0.06}^{+0.09}$, $e_{\rm gw,\ 20\ Hz}^{\rm GW151226} = 0.04_{-0.04}^{+0.05}$, and $e_{\rm gw,\ 5.5\ Hz}^{\rm GW190521} = 0.15_{-0.12}^{+0.12}$, and therefore, find no clear evidence of eccentricity in these signals.

This paper is organized as follows. In Sec. I A, we provide an overview of the eccentric model `SEOBNRv4EHM`. In Sec. II B, we introduce new initial conditions specified at an orbit-averaged orbital frequency, and in Sec. II C, we introduce an *optimized* version of the model, `SEOBNRv4EHM_opt`, and assess its performance. We present the methodology for parameter estimation in Sec. II A. In Sec. II B we demonstrate the accuracy of `SEOBNRv4EHM_opt` in the quasicircular limit, in Sec. II C we show the importance of the radial phase parameter with mock-signal injections, and in Sec. III D we asses the accuracy of the model against eccentric NR waveforms from the SXS catalog using zero noise. In Sec. III E, we analyze GW events detected by the LVK Collaboration. In Sec. III, we summarize our main conclusions and discuss future work. Finally, in the Appendix we provide details about the derivation of the expressions used in the initial conditions specified at an orbit-averaged frequency.

A. Notation

In this paper, we use geometric units, setting $G = c = 1$ unless otherwise specified.

We consider a binary with masses $m_{1,2}$, with $m_1 \geq m_2$, and spins $S_{1,2}$. We define the following combination of masses

$$M \equiv m_1 + m_2, \qquad \mu \equiv \frac{m_1 m_2}{M}, \qquad \nu \equiv \frac{\mu}{M},$$
$$\delta \equiv \frac{m_1 - m_2}{M}, \qquad q \equiv \frac{m_1}{m_2}. \tag{1}$$

A relevant combination of masses for GW data analysis is the *chirp mass* defined as [115]

$$\mathcal{M} = \nu^{3/5} M. \tag{2}$$

For nonprecessing configurations the spin components are aligned/anti-aligned with the orbital angular momentum, L, with direction $\hat{L}$. In this case the dimensionless spin components can be defined as

$$\chi_i = S_i \cdot \hat{L} / m_i^2, \tag{3}$$

where i = 1, 2. It is convenient to define the effective-spin parameter χ_{eff} [92,116,117],

$$\chi_{\text{eff}} = \frac{1}{M}(m_1\chi_1 + m_2\chi_2), \tag{4}$$

and the spin combinations,

$$\chi_S = \frac{1}{2}(\chi_1 + \chi_2), \qquad \chi_A = \frac{1}{2}(\chi_1 - \chi_2). \tag{5}$$

II. ECCENTRIC EFFECTIVE-ONE-BODY WAVEFORM MODEL WITH NONPRECESSING SPINS

In this section we describe the waveform model, SEOBNRv4EHM, used throughout the paper. We provide an overview of the model, develop a new procedure to specify the initial conditions at an orbit-averaged frequency, and introduce modifications to increase the computational efficiency of the model.

A. Overview

The SEOBNRv4EHM model was presented in Ref. [101], and we refer therein for further details. SEOBNRv4EHM is constructed within the EOB formalism [89–93], and thus it is constituted by three main building blocks:

(i) EOB *Hamiltonian*: The EOB conservative dynamics is determined by the EOB Hamiltonian constructed from the effective Hamiltonian, H_{eff}, as described in Refs. [118,119], augmented with the parameters $(K, d_{\text{SO}}, d_{\text{SS}}, \Delta t_{\text{peak}}^{22})$ calibrated to NR waveforms from Ref. [120], through the energy map [89]

$$H_{\text{EOB}} = M\sqrt{1 + 2\nu\left(\frac{H_{\text{eff}}}{\mu} - 1\right)}. \tag{6}$$

For spins antialigned/aligned with the orbital angular momentum the motion is restricted to a plane. As a consequence, the dynamical variables in the Hamiltonian are the (dimensionless) radial separation $r \equiv R/M$, the orbital phase ϕ, and their (dimensionless) conjugate momenta $p_r \equiv P_r/\mu$ and $p_\phi \equiv P_\phi/\mu$.

(ii) *Radiation-reaction force*: The dissipative effects in the EOB dynamics are described by a radiation-reaction (RR) force $\mathcal{F}$, which enters the Hamilton equations of motion, as [121,122]

$$\dot{r} = \xi(r)\frac{\partial \hat{H}_{\text{EOB}}}{\partial p_{r_*}}(r, p_{r_*}, p_\phi),$$

$$\dot{\phi} = \frac{\partial \hat{H}_{\text{EOB}}}{\partial p_\phi}(r, p_{r_*}, p_\phi),$$

$$\dot{p}_{r_*} = -\xi(r)\frac{\partial \hat{H}_{\text{EOB}}}{\partial r}(r, p_{r_*}, p_\phi) + \hat{\mathcal{F}}_r, \quad \dot{p}_\phi = \hat{\mathcal{F}}_\phi, \tag{7}$$

where the dot represents the time derivative $d/d\hat{t}$, with respect to the dimensionless time $\hat{t} \equiv T/M$, $\hat{H}_{\text{EOB}} \equiv H_{\text{EOB}}/\mu$, and $\hat{\mathcal{F}}_\phi \equiv \mathcal{F}_\phi/M$.

The equations are expressed in terms of $p_{r_*} \equiv p_r \xi(r)$, which is the conjugate momentum to the tortoise-coordinate r_*, and $\xi(r) \equiv dr/dr_*$ can be expressed in terms of the potentials of the effective Hamiltonian [121]. The components of the RR force are computed using the following relations [90,93]

$$\hat{\mathcal{F}}_\phi = -\frac{\Phi_E}{\omega}, \qquad \hat{\mathcal{F}}_r = \hat{\mathcal{F}}_\phi \frac{p_r}{p_\phi}, \tag{8}$$

where $\omega = \dot{\phi}$ is the (dimensionless) orbital frequency, and Φ_E is the energy flux for quasicircular orbits written as a sum over waveform modes using [123,124]

$$\Phi_E = \frac{\omega^2}{16\pi} \sum_{l=2}^{8} \sum_{m=-l}^{l} m^2 \left|\frac{d_L}{M}h_{lm}\right|^2, \tag{9}$$

where d_L is the luminosity distance between the binary system and the observer.

(iii) *Waveform multipoles*: The GW multipoles are composed by two main parts: the inspiral-plunge multipoles $h_{lm}^{\text{insp-plunge}}$, and the merger-ringdown $h_{lm}^{\text{merger-RD}}$ modes,

$$h_{\ell m}(t) = \begin{cases} h_{\ell m}^{\text{insp-plunge}}(t), & t < t_{\text{match}}^{\ell m} \\ h_{\ell m}^{\text{merger-RD}}(t), & t > t_{\text{match}}^{\ell m}, \end{cases} \tag{10}$$

where $t_{\text{match}}^{\ell m}$ is defined from the peak of the amplitude of the (2,2)-mode (see Ref. [102] for details). The merger-ringdown modes of SEOBNRv4EHM are the same as in the underlying SEOBNRv4HM model [102,120], and thus we assume that the effects of eccentricity at merger-ringdown are negligible. The inspiral-plunge multipoles are constructed upon the NR-calibrated quasicircular SEOBNRv4HM multipoles [102] by incorporating the 2PN eccentric corrections, including spin-orbit and spin-spin effects, as derived in Ref. [100], and are augmented by an orbit-averaged procedure to compute the

nonquasicircular (NQC) terms (see Sec. I A B from Ref. [101] for details).

B. New eccentric initial conditions

The initial conditions of SEOBNRv4EHM are expressed in terms of the eccentricity, e, and the relativistic anomaly ζ defined in the Keplerian parametrization of the orbit [101]

$$r = \frac{1}{u_p(1 + e\cos\zeta)}, \qquad (11)$$

where u_p is the inverse semilatus rectum. Given the masses, spins, the initial instantaneous orbital frequency ω_0, initial eccentricity e_0 and relativistic anomaly ζ_0, the initial conditions for r_0 and $p_{\phi 0}$, in absence of radiation reaction, can be obtained by solving the equations [101]

$$\left[\frac{\partial \hat{H}_{\mathrm{EOB}}}{\partial r}\right]_0 = -[\dot{p}_r(p_\phi, e, \zeta)]_0, \qquad \left[\frac{\partial \hat{H}_{\mathrm{EOB}}}{\partial p_\phi}\right]_0 = \omega_0, \qquad (12)$$

with $p_r(p_\phi, e, \zeta)$ and $\dot{p}_r(p_\phi, e, \zeta)$ given by the 2PN-order expressions in Eqs. (C3) and (C4) of the Appendix C in Ref. [101].

The initial condition for p_{r_0} can be computed using the solution for r_0 and $p_{\phi 0}$, and numerically solving

$$\left[\frac{\partial \hat{H}_{\mathrm{EOB}}}{\partial p_r}\right]_0 = [\dot{r}^{(0)} + \dot{r}^{(1)}]_0, \qquad (13)$$

where $\dot{r}^{(0)}$ is the 2PN-order expression for $\dot{r}$ at zeroth order in the RR effects (see Eq. (C5) in Ref. [101]), while $\dot{r}^{(1)}$ is the first-order term in the RR part of $\dot{r}$, for which we use the quasicircular expression derived in Ref. [93]

$$\dot{r}^{(1)} = -\frac{\Phi_E^{\mathrm{qc}}}{\omega}\frac{\partial^2 \hat{H}_{\mathrm{EOB}}/\partial r \partial p_\phi}{\partial^2 \hat{H}_{\mathrm{EOB}}/\partial r^2}, \qquad (14)$$

being Φ_E^{qc} the quasicircular energy flux given in Eq. (9). Finally, the initial value p_{r_0} is converted into the tortoise-coordinate conjugate momentum $p_{r_* 0}$, using the relations in Sec. II A of Ref. [101], so that together with r_0 and $p_{\phi 0}$, it can be introduced in Eq. (7) to evolve the EOB equations of motion.

The specification of eccentricity and relativistic anomaly at an instantaneous orbital frequency, which enters the right-hand side (RHS) of Eq. (12), implies significant variations of the length of the EOB dynamics (and thus of the waveform length), as one of the eccentric parameters is modified. This effect is displayed in Fig. 1 for the orbital frequency evolution for a configuration with mass ratio $q = 3$, dimensionless spins $\chi_1 = 0.3$, $\chi_2 = 0.5$, and total mass $70 M_\odot$ at a starting frequency of 20 Hz. In particular, we show in the upper panel of Fig. 1, the instantaneous orbital frequency at a fixed initial eccentricity, $e_0 = 0.2$,
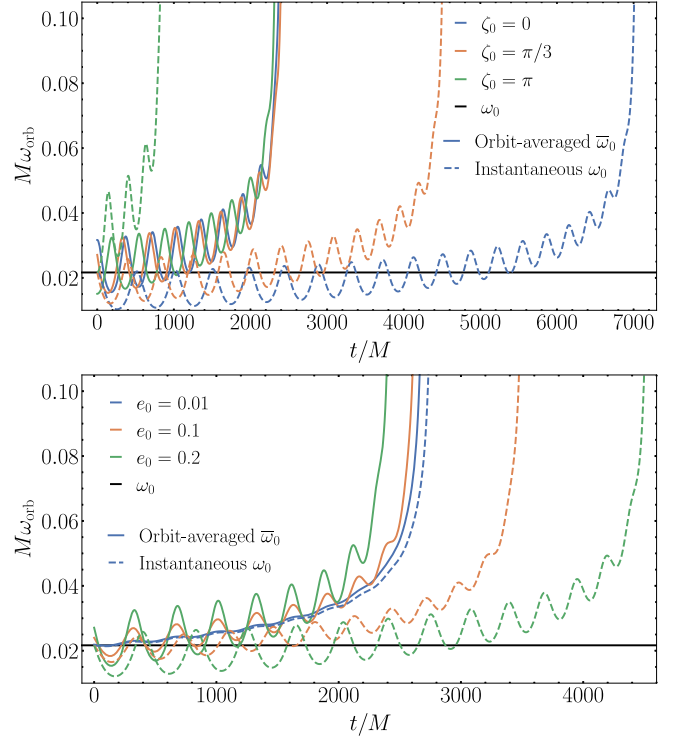

FIG. 1. Top panel: orbital frequency evolution of SEOBNRv4EHM for a configuration with mass ratio $q = 3$, dimensionless spins $\chi_1 = 0.3$, $\chi_2 = 0.5$, $e_0 = 0.2$, total mass $70 M_\odot$ at a starting frequency of 20 Hz, and three different values of initial relativistic anomaly $\zeta_0 = [0, \pi/3, \pi]$. The dashed curves correspond to the specification of (e_0, ζ_0) at an instantaneous orbital frequency, ω_0, while the solid lines correspond to the initial conditions specified at an orbit-averaged orbital frequency $\bar{\omega}_0$. Bottom panel: same configuration as in the upper panel, but fixing $\zeta_0 = \pi/3$, and using three different values of initial eccentricity, $e_0 = [0.01, 0.1, 0.2]$, for both types of initial conditions. The horizontal black solid line in both panels indicates a dimensionless frequency of $M\omega_0 = 0.0216$, corresponding to 20 Hz at $70 M_\odot$.

for three values of the initial relativistic anomaly, $\zeta_0 = [0, \pi/3, \pi]$ (dashed lines). Imposing that the initial eccentricity and relativistic anomaly are specified at an instantaneous orbital frequency causes necessarily that the length of the evolution is substantially different when the initial relativistic anomaly is at periastron ($\zeta_0 = 0$) or apastron ($\zeta_0 = \pi$). In the bottom panel of Fig. 1, we display the instantaneous orbital frequency for three values of initial eccentricity, $e_0 = [0.01, 0.1, 0.2]$, at a fixed value of the initial relativistic anomaly ($\zeta_0 = \pi/3$). The evolutions (dashed lines) show that the higher the eccentricity the longer the evolution due to the larger oscillations in the instantaneous orbital frequency, and therefore, the chosen value of ω_0 is crossed at earlier times in the inspiral.

We note that specifying the initial eccentricity and relativistic anomaly at an instantaneous orbital frequency is a particular parametrization of elliptical orbits. Other

possible parametrizations exist in the literature. For instance, in post-Newtonian (PN) models based on the quasi-Keplerian parametrization [125–141], the initial conditions for the evolution of a binary in elliptical orbits are specified at an initial orbit-averaged orbital frequency. In these evolutions the initial parameters are the orbit-averaged orbital frequency, eccentricity and radial phase (typically the mean anomaly). One of the consequences of this parametrization is that at a fixed value of eccentricity, changes in the radial phase correspond to different positions in the same orbit. While an increase (decrease) of the value of eccentricity at fixed value of the radial phase causes a decrease (increase) of the length of the evolution.

An additional motivation to explore a new parametrization of the initial conditions for SEOBNRv4EHM is the application of the model to Bayesian inference studies. Particularly, when performing parameter estimation with SEOBNRv4EHM, the usage of the initial conditions based on the instantaneous orbital frequency produce an increase in the structure of the log-likelihood surface as can be observed in Fig. 2. There, we show the log-likelihood computed for a zero-noise injection of a SEOBNRv4E waveform with initial eccentricity $e_0 = 0.1$, total mass $65 M_\odot$, and dimensionless spins $\chi_1 = 0.3$, $\chi_2 = 0$ at a starting frequency of 20 Hz, and recovering with SEOBNRv4E with all the parameters fixed to injected values except for the initial eccentricity and relativistic anomaly. We consider 5000 random points in the parameter space $\zeta_0 \in [0, 2\pi]$ and $e_0 \in [0, 0.3]$, and use the parameter estimation code BILBY [142,143] to compute the likelihood. In the uppermost panel we fix the value of the initial relativistic anomaly to periastron ($\zeta_0 = 0$) and sample only in eccentricity, while in the midpanel we fix $\zeta_0 = 1$ and sample both in initial eccentricity and relativistic anomaly. In both panels the specification of the initial conditions at an instantaneous orbital frequency leads to a complex structure in the log-likelihood values, which can pose a challenge for stochastic samplers as shown in Sec. III C.

Therefore, we introduce a new parametrization of the EOB initial conditions where the initial eccentricity and relativistic anomaly are specified at an orbit-averaged orbital frequency, $\bar{\omega}_0$. The orbit-averaged orbital frequency can be defined as

$$\bar{\omega}_0 = \frac{1}{T_r} \oint \omega(t) dt, \tag{15}$$

where T_r is the radial period. The integral in Eq. (15) can be computed using the 2PN expressions in the Keplerian parametrization from Ref. [100], and a detailed derivation can be found in the Appendix.
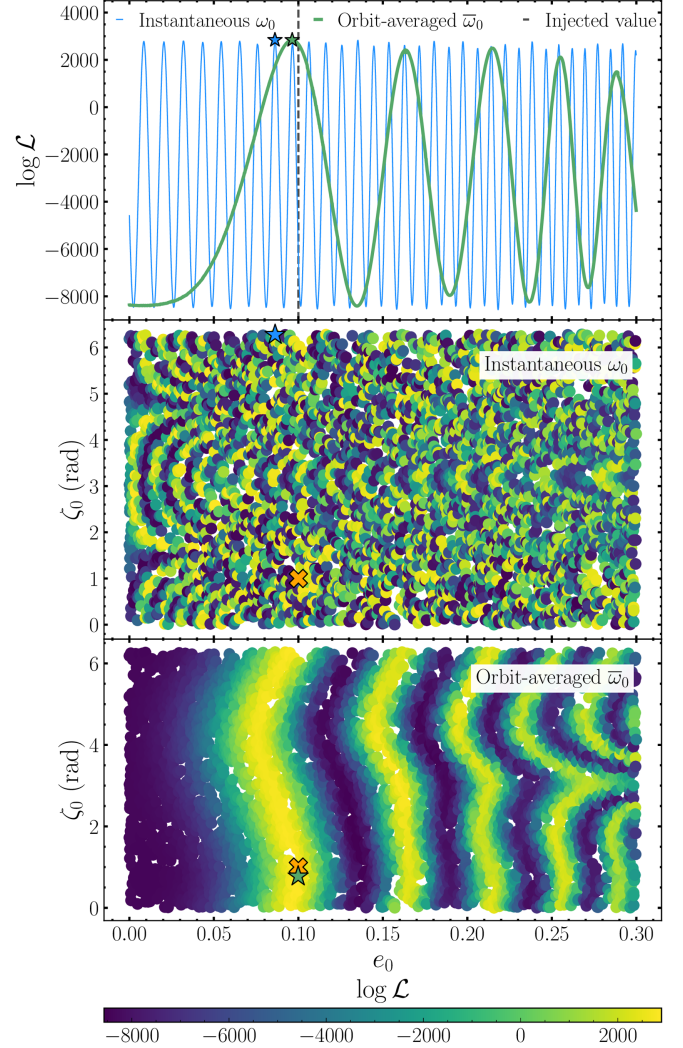

FIG. 2. Zero-noise injection of a SEOBNRv4E waveform with initial eccentricity $e_0 = 0.1$, total mass $65 M_\odot$ and spins $\chi_1 = 0.3$, $\chi_2 = 0$ at a starting frequency of 20 Hz, and recovering with SEOBNRv4E with all the parameters fixed to injected values except for the eccentric ones (e_0, ζ_0). In all the plots we consider 5000 points randomly distributed in the parameter space $\zeta_0 \in [0, 2\pi]$ and $e_0 \in [0, 0.3]$. In the top panel, the relativistic anomaly is fixed to $\zeta_0 = 0$, and only e_0 is sampled. The blue curve corresponds to using initial conditions based on the instantaneous orbital frequency, ω_0, while the green curve corresponds to using the orbit-averaged orbital frequency, $\bar{\omega}_0$. The dashed vertical line corresponds to the injected value of eccentricity. The mid and bottom plots correspond to an injected value of $\zeta_0 = 1$, and the use of ω_0 and $\bar{\omega}_0$ in the initial conditions, respectively. In both mid and bottom panels, e_0 and ζ_0 are sampled, and each point in parameter space is color-coded by its log-likelihood value. The orange crosses correspond to the injected values of eccentricity and relativistic anomaly. In all the plots the blue and green stars correspond to the maximum loglikelihood values for the instantaneous and orbit-averaged initials conditions, respectively.

The expression for $\bar{\omega}_0$ can be inverted so that the instantaneous orbital frequency is expressed in terms of the orbit-averaged frequency, eccentricity, relativistic anomaly, mass ratio and spins. Therefore, the instantaneous initial orbital frequency, ω_0, entering the RHS of Eq. (12), can be expressed as

$$
\begin{aligned}
\omega_0 = {} & \frac{\bar{\omega}_0(e\cos\zeta + 1)^2}{(1-e^2)^{3/2}} - \frac{e\bar{\omega}_0^{5/3}(3e + 2\cos\zeta)(e\cos\zeta + 1)^2}{(1-e^2)^{5/2}} - \frac{\bar{\omega}_0^2 e(e + \cos\zeta)}{(e^2 - 1)^3}(1 + e\cos\zeta)^2[2\delta\chi_A - (\nu - 2)\chi_S] \\
& - \frac{\bar{\omega}_0^{7/3}(e\cos\zeta + 1)^2}{12(1-e^2)^{7/2}}\Big\{ 12e^4(\nu - 6) + 8e(e^2(\nu - 15) - \nu + 6)\cos\zeta - 3e^2\Big[2\Big(6\sqrt{1-e^2} + 7\Big)\nu \\
& - 30\sqrt{1-e^2} + 17\Big] + 18\Big(\sqrt{1-e^2} - 1\Big)(2\nu - 5)\Big\} + \frac{e\bar{\omega}_0^{7/3}(e\cos\zeta + 1)^2}{2(1-e^2)^{7/2}}\Big\{ 2\delta\chi_A\chi_S[e(2\nu - 1)\cos(2\zeta) \\
& + 2e(\nu - 1) + (8\nu - 4)\cos\zeta] + \chi_S^2\Big[-e(2 - 4\nu + 4\nu^2 + (1 - 2\nu)^2\cos(2\zeta)) - 4(1 - 2\nu)^2\cos\zeta\Big] \\
& + (4\nu - 1)\chi_A^2[e(\cos(2\zeta) + 2) + 4\cos\zeta]\Big\} + \mathcal{O}(\bar{\omega}_0^{8/3}).
\end{aligned}
\tag{16}
$$

Given masses, spins, initial eccentricity and relativistic anomaly at a particular orbit-averaged frequency $\bar{\omega}_0$, we use Eq. (16) to compute the corresponding instantaneous orbital frequency ω_0, which enters the right-hand side (rhs) of Eq. (12). The rest of the procedure to compute the EOB initial conditions is not modified. The impact of this new parametrization in the EOB dynamics, can be observed in Fig. 1, where the solid lines correspond to the orbital frequency evolution of SEOBNRv4EHM using initial conditions specified at an orbit-averaged frequency of 20 Hz. The main effect of this new parametrization is the almost constant merger time when varying the initial relativistic anomaly at a fixed value of initial eccentricity (top panel), and the reduction of the length of the evolution with increasing e_0 at a fixed value of ζ_0 (bottom panel) due to the larger emission of radiation at periastron passages. This behavior resembles the one in PN models based on the quasi-Keplerian parametrization [132,134,137,140,141], except for the fact that the EOB initial conditions are not adiabatic as in PN, and thus causing small variations of the merger time with different values of ζ_0 at a fixed value of e_0 (see top panel of Fig. 1).

Finally, sampling in e_0 and ζ_0 at $\bar{\omega}_0$, produces notably simpler log-likelihood structures as shown in Fig. 2. In the top panel, where the sampling is performed only in e_0, the number of oscillations in the log-likelihood curves is reduced with respect to the initial conditions based on the instantaneous orbital frequency. The results of the orbit-average initial conditions create a pattern with an easy to identify maximum in log-likelihood (green curve) at the injected value of $e_0 = 0.1$ (dashed vertical line). Furthermore, we find that the maximum loglikelihood values of the orbit-average initial conditions (green star) is closer to the injected value than the instantaneous initial conditions (blue star) for a set of 5000 points. While in the bottom panel, where the sampling in e_0 and ζ_0 is performed, it emerges a clearly

defined pattern, and the values of e_0 and ζ_0 at the maximum log-likelihood point for the orbit-averaged initial conditions are $e_{\log\mathcal{L}_{\max}}^{\text{orb-avg}} = 0.099$, $\zeta_{\log\mathcal{L}_{\max}}^{\text{orb-avg}} = 0.77$ (green star in the bottom panel of Fig. 2), while for the instantaneous initial conditions are $e_{\log\mathcal{L}_{\max}}^{\text{orb-avg}} = 0.086$, $\zeta_{\log\mathcal{L}_{\max}}^{\text{orb-avg}} = 4.829$ (blue star in the mid panel of Fig. 2) is also closer to the injected values (orange crosses). An accurate recovery of the injected values requires more than 5000 points in the 2D parameter, however, the results already indicate that even with a low number of points the initial conditions based on the orbit-averaged orbital frequency are closer to the injected value, and may need less points than the recovery using the initial conditions based on the instantaneous orbital frequency. Thus, the initial conditions at an orbit-averaged frequency may be more adequate for data analysis applications such as parameter estimation, and in Sec. III C we further explore the consequences of these different initial conditions with stochastic sampling techniques.

C. Computational performance

One of the main applications of waveform models is the inference of the source parameters using Bayesian inference methods. These methods typically require of the order of $\sim 10^7$–10^8 or more waveform evaluations. The SEOBNRv4EHM model is built upon the SEOBNRv4HM model [102], and thus it inherits the low computational efficiency of the previous generation of SEOBNR models.[1] Several techniques exist to increase the computational efficiency of EOB waveforms, such as reduced-order or surrogate models [149–157], the post-adiabatic approximation [158,159], as well as methods targeting specifically

---

[1]The computational efficiency of the SEOBNR models has been recently significantly improved by the new generation of SEOBNRv5 models [144–148].

parameter estimation, such as reduced order quadratures [160–163] or relative binning [164].

Here, we decide to increase the efficiency of SEOBNRv4EHM by reducing the absolute and relative tolerances of the 4th-order Runge-Kutta integrator from 10^{-10} and 10^{-9} to 10^{-8} and 10^{-8}, respectively.[2] Furthermore, as in the SEOBNRv4EHM model the Hamiltonian and the radiation-reaction force are the same as in the SEOBNRv4HM model, we also use the optimized Hamiltonian and integrator from Refs. [103,104]. In order to ease notation we refer to the model with reduced tolerances and optimizations as SEOBNRv4EHM_opt, and SEOBNRv4E_opt when referring to the model containing only the $(l, |m|) = (2, 2)$ multipoles.

The reduction of the ODE tolerances implies an increase in the efficiency of the model with waveform evaluation timescales of the order of $\mathcal{O}(100 \text{ ms})$, while decreasing the accuracy of the model. In order to quantify the latter across parameter space, we compute the unfaithfulness between the SEOBNRv4EHM and SEOBNRv4EHM_opt models for 4500 points in the parameter space $q \in [1, 50]$, $\chi_{1,2} \in [-0.9, 0.9]$, $e_0 \in [0, 0.5]$, $\zeta_0 \in [0, 2\pi]$ for a dimensionless starting frequency of $M\omega_0 = 0.023$. We define the inner product between two waveforms, h_A and h_B [165,166]

$$\langle h_A, h_B \rangle \equiv 4 \text{Re} \int_{f_{\text{in}}}^{f_{\text{max}}} df \, \frac{\tilde{h}_A(f) \tilde{h}_B^*(f)}{S_n(f)}, \qquad (17)$$

where a tilde indicates Fourier transform, a star complex conjugation and $S_n(f)$ the power spectral density (PSD) of the detector noise. In this work, we employ for the PSD the LIGO's "ero-detuned high-power" design sensitivity curve [167]. Similarly, as in Ref. [147], we use $f_{\text{in}} = 10$ Hz and $f_{\text{max}} = 2048$ Hz.

To assess the agreement between two waveforms—for instance, the signal, h_s, and the template, h_t, observed by a detector, we define the faithfulness function [102,168],

$$\mathcal{F}(M_s, \iota_s, \varphi_{0s}) = \max_{t_c, \varphi_{0t}} \left[\left| \frac{\langle h_s | h_t \rangle}{\sqrt{\langle h_s | h_s \rangle \langle h_t | h_t \rangle}} \right|_{\substack{\iota_s = \iota_t \\ \lambda_s(t_s = t_{0s}) = \lambda_t(t_t = t_{0t})}} \right], \qquad (18)$$

where $\lambda = \{m_{1,2}, \chi_{1,2}, e_0, \zeta_0\}$ denotes the set of intrinsic parameters of the binary. When comparing waveforms, we choose the same inclination angle for the signal and template $\iota_s = \iota_t = \pi/3$, while the coalescence time and azimuthal angles of the template, (t_{0_t}, φ_{0_t}), are adjusted to maximize the faithfulness of the template. The

---

[2]The reduction of the tolerances is a similar approach to the one followed in Ref. [79] to improve the efficiency of the TEOBResumS-Dali model [99].
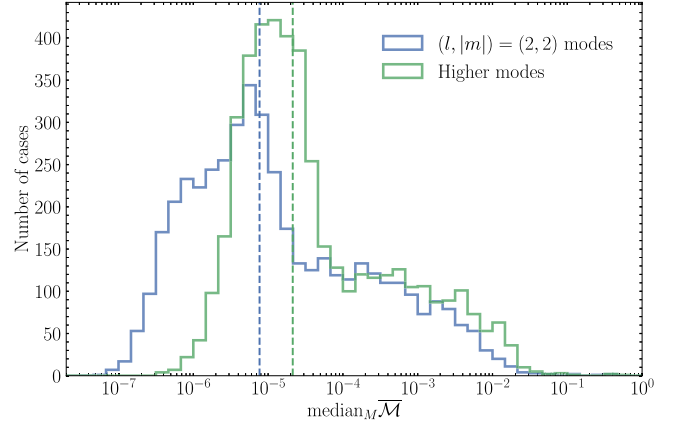

FIG. 3. Distribution of median unfaithfulness over the total mass range between $[20 - 300]M_\odot$ for an inclination $\iota = \pi/3$, between the $(l, |m|) = (2, 2)$-modes models, SEOBNRv4E and SEOBNRv4E_opt (blue), as well as between the higher-order mode models, SEOBNRv4EHM and SEOBNRv4EHM_opt (green) for 4500 configurations in the parameter space $q \in [1, 50]$, $\chi_{1,2} \in [-0.9, 0.9]$, $e_0 \in [0, 0.5]$ and $\zeta_0 \in [0, 2\pi]$ for a dimensionless starting frequency of $M\omega_0 = 0.023$. The vertical dashed lines indicate the median values of the distribution.

maximizations over the coalescence time t_c and coalescence phase φ_{0t} are performed numerically. Similarly as in Sec. IV of Ref. [147] we set a grid of 8 points in the coalescence phase of the signal $\varphi_{0s} \in [0, 2\pi]$, and average over it to compute $\mathcal{F}$. Finally, we introduce the unfaithfulness or mismatch as

$$\bar{\mathcal{M}} = 1 - \bar{\mathcal{F}}. \qquad (19)$$

In Fig. 3 we show the distribution of median unfaithfulness over the total mass range $[20 - 300]M_\odot$ between the models containing only the $(l, |m|) = (2, 2)$ modes, SEOBNRv4E and SEOBNRv4E_opt models, as well as for the models including also the subdominant harmonics, i.e., $(l, |m|) = (2, 2), (2, 1), (3, 3), (4, 4), (5, 5)$ multipoles. The results demonstrate a remarkable good agreement between the optimized (SEOBNRv4EHM_opt and SEOBNRv4E_opt) and the original models (SEOBNRv4EHM and SEOBNRv4E), with a median of unfaithfulness of 7.7×10^{-6} for the dominant mode models, and 2.1×10^{-5} for the models including higher order modes. As expected the differences between models with higher order modes are larger than for the dominant-mode models, due to the fact that small changes in the termination of the dynamics caused by the modifications in SEOBNRv4EHM_opt impact more significantly the higher multipoles. In particular, the reduced tolerances in the integration can lead to small differences in the non-quasicircular coefficients computed from the input values (see Ref. [120] for details), which affect more the higher modes due to their low power. Furthermore, we also

observe a tail of cases with unfaithfulness larger than 1% between the original and optimized models. These cases correspond to the more challenging parts of the parameter space considered with $e_0 > 0.3 - 0.5$ and high spins ($\chi_{1,2} > 0.8 - 0.9$), where the models have known limitations, such as the orbit-averaged procedure (see Appendix B of Ref. [101]), and the use of nonquasicircular corrections calibrated to quasicircular binaries, which may increase the differences between the models.

Finally, we assess the computational efficiency of the SEOBNRv4EHM_opt model by timing the waveform generation and comparing it to the original SEOBNRv4EHM model, as well as the SEOBNRv4HM model in the quasicircular limit. We consider binary's configurations with mass ratio $q = 3$, dimensionless spins $\chi_1 = -0.5, \chi_2 = 0.3$, initial relativistic anomaly $\zeta_0 = 1$, total mass range $M \in [20, 200]M_\odot$, starting frequency $f_{\text{start}} = 10$ Hz and two different initial eccentricities $e_0 = 0, 0.2$. The results of the walltimes to generate the waveforms are shown in Fig. 4, where we are including all the modes up to $l = 4$, and a fixed sampling rate of 8192 Hz for all the total masses considered.[3] The values of the walltimes are computed as an average over 100 waveform evaluations for each value shown in Fig. 4. The outcome of the benchmark demonstrates the significant increase in speed of the SEOBNRv4EHM_opt model with respect to the SEOBNRv4EHM and SEOBNRv4HM models. For the configurations considered, we observe approximately a factor 2–5 improvement in speed. In the quasicircular limit SEOBNRv4EHM is on average, over the total mass considered, slightly (~1.5 times) faster than SEOBNRv4HM due to a more efficient implementation of some operations involved in the waveform calculation of SEOBNRv4EHM, while SEOBNRv4EHM_opt is a factor ~2.7 faster than SEOBNRv4EHM. Regarding models with only the $(l, |m|) = (2, 2)$ modes, the hierarchy of curves is similar with the SEOBNRv4E_opt being faster than SEOBNRv4E by a factor ~3.1. This increase in speed compared to models with higher-order modes is due to the lack of common operations performed for models with higher-order modes, which limit the speed of the latter. When considering an initial eccentricity $e_0 = 0.2$ in the bottom panel of Fig. 4, we find an average (over total masses) increase of speed of ~7.7 and ~3.8 for the SEOBNRv4E_opt and SEOBNRv4EHM_opt models. The speed increase is more significant at low total masses as the main cost of waveform generation comes from the evaluation of the EOB dynamics, which is computed less frequently in the optimized model due to the reduced integration tolerances.
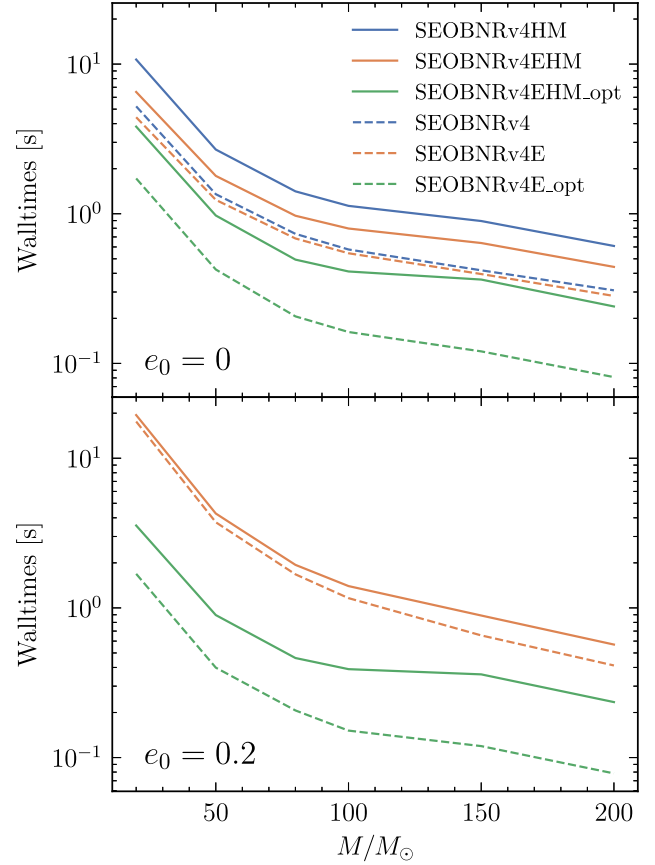

FIG. 4. Walltimes of the SEOBNRv4HM, SEOBNRv4EHM, SEOBNRv4EHM_opt models (solid lines) for a configuration with mass ratio $q = 3$, dimensionless spins $\chi_1 = -0.5, \chi_2 = 0.3$, initial relativistic anomaly $\zeta_0 = 1$, total mass range $M \in [20, 200]M_\odot$, starting frequency $f_{\text{start}} = 10$ Hz and two different initial eccentricities $e_0 = 0$ (top panel) and $e_0 = 0.2$ (bottom panel). The dashed lines correspond to the models with only the $(l, |m|) = (2, 2)$ multipoles (SEOBNRv4, SEOBNRv4E and SEOBNRv4E_opt). The walltimes are computed averaging over a hundred waveform evaluations and using a sampling rate of 8192 Hz for all the masses considered.

In summary, the SEOBNRv4E_opt and SEOBNRv4EHM_opt models imply a significant acceleration in waveform evaluation with respect to their original counterparts with a minor reduction in accuracy, in the region of parameter space of interest for our study. Furthermore, the sampling rate used for the benchmarks here is rather high[4] (8192 Hz), and typical applications for data analysis may use lower ones, which implies that the walltimes for waveform evaluation may be further reduced. As a consequence the optimized models reach speeds competitive for parameter estimation, and we show in Sec. III that

---

[3]The benchmarks of the waveform generation timing were performed on a computing node (dual-socket, 128-cores per socket, SMT-enabled AMD EPYC (Milan) 7742 (1.5 GHz), with 4 GB RAM per core) of the Hypatia cluster at the Max Planck Institute for Gravitational Physics in Potsdam.

[4]We choose such a sampling rate value in order to resolve all the modes up to $l = 4$ for all the total mass range considered, $M \in [20, 200]M_\odot$.

they can be used to perform parameter-estimation runs in the order of hours and days.

III. BAYESIAN INFERENCE STUDY

The main application of the SEOBNRv4EHM_opt waveform model is the Bayesian inference of source parameters of GWs emitted by BBHs. Thus, we introduce the methods and parameter-estimation codes used to infer the binary parameters in Sec. III A, we show the accuracy of the model in the quasicircular limit in Sec. III B, we assess in Sec. III C the impact of the different initial conditions discussed in Sec. II B, as well as the importance of the relativistic- anomaly parameter. In Sec. III D we further investigate the accuracy of the model by performing a series of synthetic NR signal injections into zero detector noise. Finally, in Sec. III E, we analyze three real GW events detected by the LVK collaboration (GW150914, GW151226 and GW190521), and compare with results from the literature.

A. Methodology for parameter estimation

For the parameter-estimation study we employ PARALLEL BILBY[5] [105], a highly parallelized version of the Bayesian inference Python package BILBY [142,143], incorporating the nested sampler DYNESTY [169]. Based on previous experience with PARALLEL BILBY [147], we use a number of autocorrelation times nact = 30, number of live points nlive = 2048, and the remaining sampling parameters with their default values, unless otherwise specified. Furthermore, the runs are performed using distance marginalization as implemented in BILBY, and the phase marginalization is activated when using the $(l, |m|) = (2, 2)$-mode models to further reduce the computational cost.

For the choice of priors, we follow broadly Refs. [1,147,170]. We choose a prior in inverse mass ratio, $1/q$, and chirp mass, $\mathcal{M}$, such that it is uniform in component masses. The priors in initial eccentricity, e_0, and relativistic anomaly, $\zeta_0 \in [0, 2\pi]$, are chosen to be uniform. In order to facilitate the comparison with precessing-spin results, the priors on the spin-components, $\chi_{1,2}$, are chosen such that they correspond to the projections of a uniform and isotropic spin distribution along the $\hat{z}$-direction [170]. The luminosity distance prior is chosen to be proportional to $\propto d_L^2$, unless otherwise specified. The rest of the priors are set according to Appendix C of Ref. [1]. The specific values of the prior boundaries for the different parameters vary depending on the application, and we specify them in the subsequent sections.

B. Quasicircular limit

Eccentricity is a parameter, which defines the ellipticity of an orbit between two limits: the parabolic and the circular case. In this section we consider the latter, and demonstrate that the SEOBNRv4EHM_opt model is able to accurately describe GWs from quasicircular BBHs. In Sec. III of Ref. [101] it is shown that SEOBNRv4EHM has a comparable accuracy to SEOBNRv4HM by computing the unfaithfulness against quasicircular NR waveforms.

Here, we assess the accuracy of SEOBNRv4EHM_opt in the zero-eccentricity limit by computing the unfaithfulness, as defined in Sec. II C, against the accurate quasicircular SEOBNRv4HM model for 4500 random points distributed in the following parameter space: $q \in [1, 50]$, $\chi_{1,2} \in [-0.9, 0.9]$, with an inclination angle of $\iota = \pi/3$, for a total mass range $[20 - 300]M_\odot$ and starting frequency of $M\omega_0 = 0.023$ in geometric units. In Fig. 5 we show the distribution of the median unfaithfulness over the total mass range considered when comparing the $(l, |m|) = (2, 2)$-mode models, SEOBNRv4 and SEOBNRv4E_opt, as well as the corresponding models including higher multipoles, SEOBNRv4HM and SEOBNRv4EHM_opt. For SEOBNRv4E_opt the median value of unfaithfulness is 8.1×10^{-6}, while when including higher order modes it degrades to 3.8×10^{-5}. In both cases there are no configurations with unfaithfulness larger than 1%. Therefore, both the SEOBNRv4E_opt and SEOBNRv4EHM_opt models are faithful across parameter space to the SEOBNRv4 and SEOBNRv4HM models, respectively, considering that SEOBNRv4 was calibrated to NR with unfaithfulness below 1%.
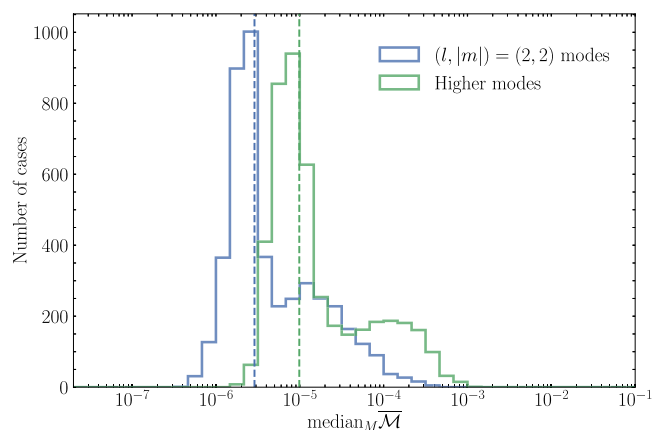

FIG. 5. Distribution of median unfaithfulness over the total mass range between $[20 - 300]M_\odot$ for an inclination $\iota = \pi/3$, between the $(l, |m|) = (2, 2)$-modes models, SEOBNRv4E_opt and SEOBNRv4 (blue), as well as between the higher-order mode models, SEOBNRv4EHM_opt and SEOBNRv4HM (green) for 4500 configurations in the parameter space $q \in [1, 50]$, $\chi_{1,2} \in [-0.9, 0.9]$ for a dimensionless starting frequency of $M\omega_0 = 0.023$. The vertical dashed lines indicate the median values of the distribution.

---

[5]In this paper we employ the PARALLEL BILBY code from the public repository https://git.ligo.org/lscsoft/parallel_bilby with the git hash b56d25b87b3b33b33a91a8410ae3a6c2a5 c92a2e, which corresponds to the version 2.0.2.
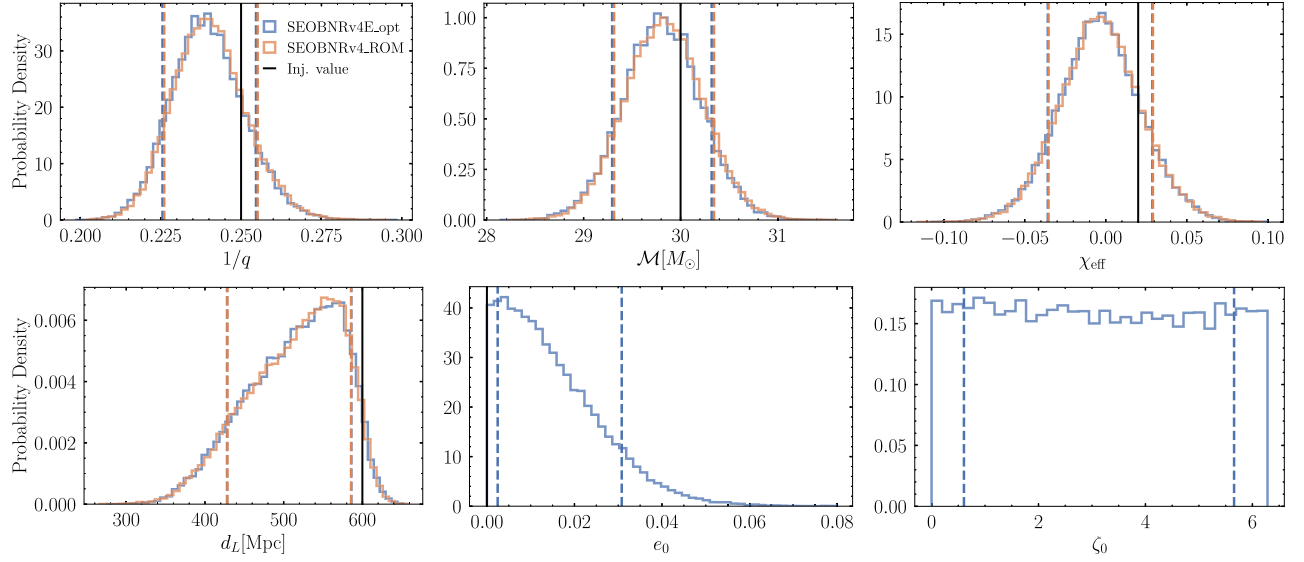
FIG. 6. Inverse mass ratio, chirp mass, effective spin parameter, luminosity distance, initial eccentricity and relativistic anomaly posterior distributions for a synthetic quasicircular BBH signal injection using the SEOBNRv4 model, and recovering the parameters with SEOBNRv4E_opt (blue) and SEOBNRv4_ROM (orange). The dashed vertical lines indicate the 90% credible intervals. The solid vertical lines correspond to the injected parameters, which are also shown in Table I.

We further investigate the implications of these unfaithfulness results in parameter estimation by performing a mock-signal injection into zero-detector noise. With zero noise, and flat priors, the likelihood will peak at the true parameters when using the same model for injection and recovery. This makes it easier to see biases that are arising from model differences. We use the SEOBNRv4 model as a signal, and recover the injected parameters with the reduced order model (ROM) SEOBNRv4_ROM [120] and the SEOBNRv4E_opt model. For the latter we also sample in initial eccentricity and relativistic anomaly. We consider a configuration with mass ratio $q = 4$, total mass $M = 90.08 M_\odot$ and BH's dimensionless spins $\chi_1 = 0.5$ and $\chi_2 = -0.1$ defined at 20 Hz.

For this injection we choose the inclination with respect to the line of sight of the BBH to be $\iota = 0.1$ rad, coalescence and polarization phases are $\phi = 0.6$ rad and $\psi = 0.33$ rad, respectively. The luminosity distance to the source is chosen to be 600 Mpc, which produces a three-detector (LIGO Hanford, LIGO Livingston and Virgo) network-SNR of $\rho_{\mathrm{mf}}^N = 67.9$ when using the LIGO and Virgo PSD at design sensitivity [167].

We choose a uniform prior in inverse mass ratio and chirp mass, with ranges $1/q \in [0.05, 1]$ and $\mathcal{M} \in [5, 100] M_\odot$. The priors on the magnitudes of the dimensionless z-components of the spins are $a_i \in [0, 0.99]$. For SEOBNRv4E_opt we take a uniform prior in the initial eccentricity $e_0 \in [0, 0.3]$, and uniform in the initial relativistic anomaly $\zeta_0 \in [0, 2\pi]$.

The resulting posteriors for the inverse mass ratio, chirp mass, effective-spin parameter, luminosity distance, initial eccentricity and relativistic anomaly are shown in Fig. 6. We find remarkable agreement between the posteriors of

SEOBNRv4E_opt and SEOBNRv4_ROM for all the parameters. The injected values and recovered parameters are displayed in Table I, where additional parameters are shown. Even for a relatively high SNR injection ($\rho_{\mathrm{mf}}^N \sim 68$) both models are able to accurately recover the injected parameters for the inverse mass ratio, chirp mass and effective-spin parameter within the 90% credible intervals,

TABLE I. Injected and median values of the posterior distributions for the synthetic injection with the SEOBNRv4 model, recovered with SEOBNRv4E_opt and SEOBNRv4_ROM. The median values also report the 90% credible intervals. The binary parameters correspond to the total mass M, chirp mass $\mathcal{M}$, inverse mass ratio $1/q$, effective-spin parameter χ_{eff}, initial eccentricity e_0, initial relativistic anomaly ζ_0, angle between the total angular momentum and the line of sight θ_{JN}, luminosity distance d_L, coalescence phase ϕ_{ref} and the network matched-filtered SNR for LIGO-Hanford/Livingston and Virgo detectors ρ_{mf}^N.

Parameter	Injected value	SEOBNRv4E_opt	SEOBNRv4_ROM
$M/M_\odot$	90.08	$90.96^{+1.44}_{-1.51}$	$90.95^{+1.42}_{-1.5}$
$\mathcal{M}/M_\odot$	30.00	$29.81^{+0.51}_{-0.51}$	$29.83^{+0.52}_{-0.51}$
$1/q$	0.25	$0.24^{+0.02}_{-0.02}$	$0.24^{+0.02}_{-0.02}$
χ_{eff}	0.02	$0.00^{+0.03}_{-0.03}$	$0.00^{+0.03}_{-0.03}$
e_0	0	$0.01^{+0.02}_{-0.01}$	$\cdots$
ζ_0	$\cdots$	$3.09^{+2.57}_{-2.48}$	$\cdots$
θ_{JN}	0.1	$0.52^{+0.29}_{-0.3}$	$0.51^{+0.29}_{-0.30}$
d_L	600	521.35^{+64}_{-93}	523^{+63}_{-94}
ϕ_{ref}	0.1	$3.15^{+2.53}_{-2.52}$	$3.16^{+2.54}_{-2.52}$
ρ_{mf}^N	67.98	$64.34^{+0.06}_{-0.06}$	$64.42^{+0.02}_{-0.03}$

while the luminosity distance presents a small bias due to the limited mode content of both models (only the $(l, |m|) = (2, 2)$ multipoles), which creates a degeneracy between the inclination angle and the luminosity distance and thus, complicates the measurement of both quantities [102,171–173]. This degeneracy and, thus the bias, can be removed by including higher multipoles in the waveform, but we do not use models with higher multipoles, as the focus of this injection study is the assessment of the agreement between the SEOBNRv4E_opt and SEOBNRv4_ROM models.

Regarding initial eccentricity and relativistic anomaly, SEOBNRv4E_opt measures an initial eccentricity consistent with zero, $e_0 = 0.01^{+0.02}_{-0.01}$, while the initial relativistic anomaly becomes an uninformative parameter as for quasicircular orbits the radial phase provides no information about the position of the binary components.

In conclusion, the SEOBNRv4EHM_opt model has an accurate zero eccentricity limit comparable to the underlying quasicircular SEOBNRv4HM model. This is extremely important as eccentricity is a gauge dependent parameter in general relativity between two well-defined limits (circular and parabolic), and being able to unambiguously recover one of them ensures that the values of eccentricity can be quoted with respect to a uniquely defined physical configuration.[6]

C. Eccentric case

Two different initial conditions (ICs) for the SEOBNRv4EHM model were presented in Sec. II B: (1) one based on the specification of the initial eccentricity and relativistic anomaly, (e_0, ζ_0) at an instantaneous orbital frequency ω_0, hereafter referred as *instantaneous* ICs, and (2) one based on the specification of (e_0, ζ_0) at an orbit-averaged orbital frequency $\bar{\omega}_0$, hereafter called *orbit-averaged* ICs.

Here, we study the implications of these ICs by performing two mock-signal injections in zero detector noise using the SEOBNRv4E_opt model as a signal with two different initial eccentricities $e_0 = [0.1, 0.2]$, and recovering with the SEOBNRv4E_opt model. We consider a configuration with mass ratio $q = 3$, initial relativistic anomaly $\zeta_0 = 1.2$, total mass $M = 76.4 M_\odot$ and BH's dimensionless spins $\chi_1 = 0.5$ and $\chi_2 = -0.1$ defined at a starting frequency of 20 Hz.[7]

The priors on the sampling parameters are chosen as in Sec. III B. The injection and recovery of the parameters are performed using the SEOBNRv4E_opt model with orbit-averaged and instantaneous ICs. Furthermore, we also

assess the importance of the relativistic anomaly parameter, ζ_0, by recovering the parameters by setting the initial starting point of the orbit at periastron ($\zeta_0 = 0$), which is different from the injected value $\zeta_0 = 1.2$. For completeness we also measure the binary parameters in the quasicircular limit ($e_0 = 0$). The resulting posterior distributions of the different cases are shown in Fig. 7 for the inverse mass-ratio, initial eccentricity and initial relativistic anomaly. The injected values, the median values and 90% credible intervals of the posterior distributions of some parameters are provided in Table II.

The left side of the violin plots in Fig. 7 shows the comparison of the orbit-averaged and instantaneous ICs as well as the zero-eccentricity case. We find that both ICs are able to accurately recover the injected parameters for all the parameters of the two injected eccentricities, $e_0 = 0.1$ and $e_0 = 0.2$. In the case of the instantaneous ICs the ζ_0 posterior is sharply peaked at the injected value due to the fact that for these ICs a change in ζ_0 at a fixed value of e_0 provides a completely different evolution, while for the orbit-averaged ICs variations of ζ_0 at a fixed value e_0 describe different values of the radial phase in the same orbit as shown in Fig. 1. These different descriptions of the orbits have also implications in the efficiency of the sampler and the cost of the parameter estimation runs. For instance, the $e_0 = 0.2$ injections were performed with the same sampler settings as described in Sec. III A and using 6 nodes of 32 cores each[8] with an averaged wall clock time of 11.8 and 35.7 hours for the orbit-averaged and instantaneous ICs, respectively. This demonstrates that the orbit-averaged ICs lead to a more computationally efficient sampling of the parameter space than the instantaneous ICs without a loss of accuracy.

We focus now on the right side of the violin plots in Fig. 7, where the results of setting the initial relativistic-anomaly parameter to a different value ($\zeta_0 = 0$) from the injected one ($\zeta_0 = 1.2$) for both the instantaneous and the orbit-averaged ICs are displayed. For the orbit-averaged ICs, neglecting the relativistic anomaly parameter can lead to biases in the quasicircular parameters like the inverse mass ratio, while the eccentricity parameter is accurately recovered (see right-side distributions in Fig. 7). This can be explained by the fact that during the parameter-estimation run the template waveform compensates the lack of another eccentric degree of freedom by modifying the rest of the parameters in order to describe more accurately the signal. This points out the relevance of taking into account the radial-phase parameter when using orbit-averaged ICs, and is in agreement with the findings of Ref. [176] during the construction of an eccentric

---

[6]For instance, in the TEOBResumS family of waveform models [158,174], Ref. [85] found a small bias between the quasicircular TEOBResumS-GIOTTO [175] and the eccentric TEOBResumS-Dali [99] models in the quasicircular limit.

[7]The starting frequency of the injected signal is orbit-average or instantaneous in order to be consistent with the ICs used for the recovery of the parameters.

[8]The parameter estimation runs were performed using computing nodes (dual-socket, 16-cores per socket, SMT-enabled AMD EPYC (Milan) 7351 (2.4 GHz), with 8 GB RAM per core) of the Hypatia cluster at the Max Planck Institute for Gravitational Physics in Potsdam.
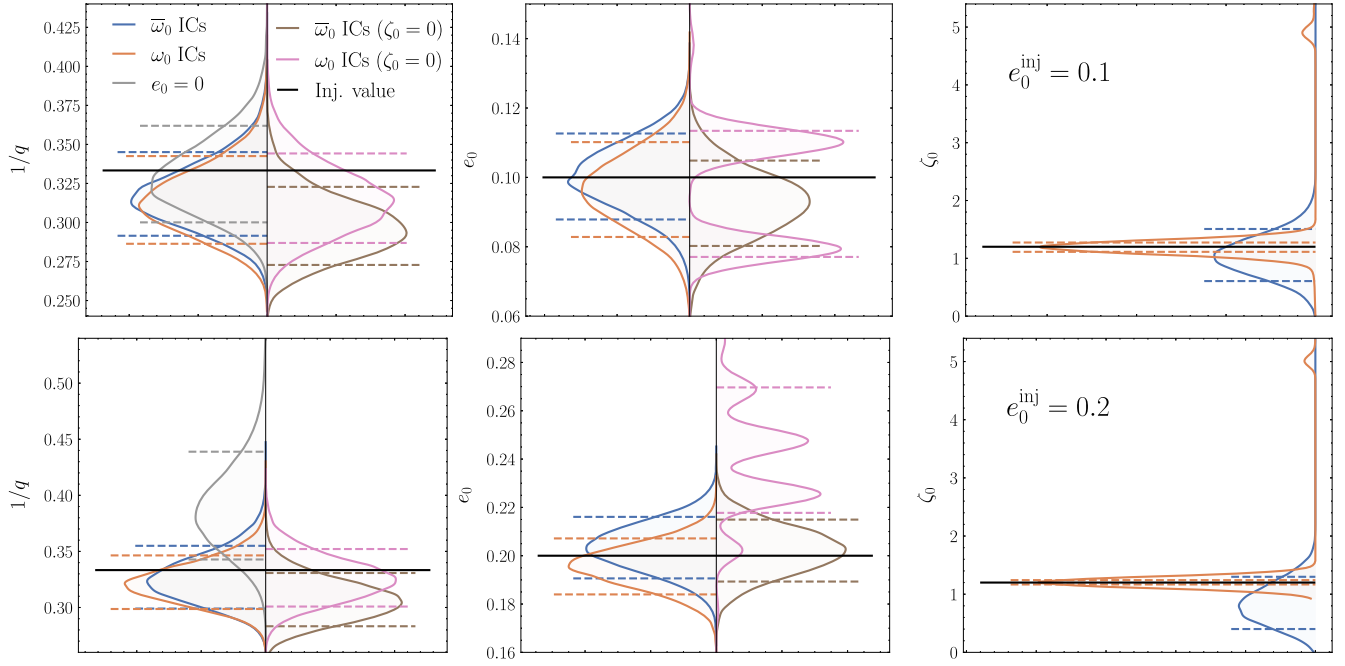
FIG. 7. Top row: Violin plots for the posterior distributions of the inverse mass ratio, initial eccentricity and relativistic anomaly for a synthetic BBH signal injection using the SEOBNRv4E_opt model with $e_0 = 0.1$ and $\zeta_0 = 1.2$ at 20 Hz. The posteriors are computed using the SEOBNRv4E_opt model with orbit-averaged ICs (blue), instantaneous ICs (orange), setting $\zeta_0 = 0$ for the orbit-averaged (brown) and instantaneous (pink) ICs, and for the zero-eccentricity case $e_0 = 0$ (gray). The cases where ζ is fixed during sampling ($\zeta_0 = 0$) have been placed on the right side of the x-axis to ease the visualization of the results. The dashed vertical lines indicate the 90% credible intervals. The solid vertical lines correspond to the injected parameters, which are also shown in Table I. Bottom row: same as in the upper row but for an injected signal with initial eccentricity $e_0 = 0.2$ at 20 Hz.

TABLE II. Injected and median values of the posterior distributions for two synthetic injections with the SEOBNRv4E_opt model with initial eccentricities $e_0 = [0.1, 0.2]$. The median values also report the 90% credible intervals. The binary parameters correspond to the total mass M, chirp mass $\mathcal{M}$, inverse mass ratio $1/q$, effective spin parameter $\chi_{\rm eff}$, initial eccentricity e_0, initial relativistic anomaly ζ_0, angle between the total angular momentum and the line of sight $\theta_{\rm JN}$, luminosity distance d_L, coalescence phase $\phi_{\rm ref}$ and the network matched-filtered SNR for LIGO-Hanford/Livingston and Virgo detectors $\rho_{\rm mf}^{\rm N}$. For each injection the recovery is done with the SEOBNRv4E_opt model using orbit-averaged ICs ($\bar\omega_0$ ICs), instantaneous ICs (ω_0 ICs), and setting $\zeta_0 = 0$ for both the orbit-averaged and instantaneous ICs, $\bar\omega_0$ ICs ($\zeta_0 = 0$) and $\bar\omega_0$ ICs ($\zeta_0 = 0$), respectively. Additionally, the values recovered setting the initial eccentricity to zero, $e_0 = 0$, are also shown.

Parameter	$M/M_\odot$	$\mathcal{M}/M_\odot$	$1/q$	$\chi_{\rm eff}$	e_0	ζ_0	$\theta_{\rm JN}$	d_L	$\phi_{\rm ref}$	$\rho_{\rm mf}^{\rm N}$
Injected value	76.45	28.0	0.33	-0.22	**0.1**	1.2	0.1	800.0	0.1	46.3
$\bar\omega_0$ ICs	$77.93^{+1.82}_{-1.88}$	$28.09^{+0.57}_{-0.59}$	$0.32^{+0.03}_{-0.02}$	$-0.23^{+0.05}_{-0.05}$	$0.1^{+0.01}_{-0.01}$	$1.04^{+0.46}_{-0.44}$	$0.53^{+0.32}_{-0.32}$	$699.63^{+96.27}_{-140.91}$	$3.14^{+2.52}_{-2.52}$	$46.3^{+0.04}_{-0.06}$
ω_0 ICs	$77.67^{+1.84}_{-1.91}$	$27.9^{+0.64}_{-0.68}$	$0.31^{+0.03}_{-0.03}$	$-0.24^{+0.05}_{-0.06}$	$0.1^{+0.01}_{-0.01}$	$1.2^{+0.07}_{-0.09}$	$0.53^{+0.32}_{-0.31}$	$691.15^{+96.25}_{-140.43}$	$3.12^{+2.51}_{-2.53}$	$46.24^{+0.04}_{-0.07}$
$\bar\omega_0$ ICs ($\zeta_0 = 0$)	$76.01^{+1.69}_{-1.63}$	$26.84^{+0.4}_{-0.43}$	$0.3^{+0.03}_{-0.02}$	$-0.31^{+0.04}_{-0.05}$	$0.09^{+0.01}_{-0.01}$	$\cdots$	$0.54^{+0.32}_{-0.31}$	$650.18^{+89.02}_{-126.32}$	$3.15^{+2.69}_{-2.51}$	$46.23^{+0.04}_{-0.07}$
ω_0 ICs ($\zeta_0 = 0$)	$77.86^{+1.9}_{-1.95}$	$27.99^{+0.65}_{-0.67}$	$0.31^{+0.03}_{-0.03}$	$-0.24^{+0.05}_{-0.05}$	$0.1^{+0.01}_{-0.03}$	$\cdots$	$0.53^{+0.32}_{-0.32}$	$697.18^{+97.41}_{-139.64}$	$3.15^{+2.48}_{-2.56}$	$46.08^{+0.04}_{-0.06}$
$e_0 = 0$	$77.01^{+2.07}_{-2.16}$	$28.07^{+0.54}_{-0.55}$	$0.33^{+0.03}_{-0.03}$	$-0.23^{+0.05}_{-0.05}$	$\cdots$	$\cdots$	$0.54^{+0.32}_{-0.32}$	$715.39^{+99.1}_{-145.79}$	$3.14^{+2.49}_{-2.52}$	$45.39^{+0.03}_{-0.05}$
Injected value	76.45	28.0	0.33	-0.22	**0.2**	1.2	0.1	800.0	0.1	46.75
$\bar\omega_0$ ICs	$78.37^{+2.23}_{-2.18}$	$28.49^{+0.51}_{-0.53}$	$0.33^{+0.03}_{-0.03}$	$-0.21^{+0.05}_{-0.05}$	$0.2^{+0.01}_{-0.01}$	$0.82^{+0.48}_{-0.42}$	$0.53^{+0.32}_{-0.32}$	$716.81^{+96.1}_{-142.65}$	$3.17^{+2.51}_{-2.53}$	$46.65^{+0.04}_{-0.06}$
ω_0 ICs	$77.31^{+1.81}_{-1.78}$	$28.0^{+0.65}_{-0.63}$	$0.32^{+0.03}_{-0.02}$	$-0.24^{+0.06}_{-0.06}$	$0.2^{+0.01}_{-0.01}$	$1.21^{+0.04}_{-0.04}$	$0.53^{+0.32}_{-0.31}$	$698.53^{+95.21}_{-141.05}$	$3.16^{+2.49}_{-2.55}$	$47.07^{+0.04}_{-0.07}$
$\bar\omega_0$ ICs ($\zeta_0 = 0$)	$77.08^{+2.06}_{-1.93}$	$27.49^{+0.34}_{-0.35}$	$0.31^{+0.02}_{-0.02}$	$-0.26^{+0.04}_{-0.04}$	$0.2^{+0.01}_{-0.01}$	$\cdots$	$0.54^{+0.31}_{-0.32}$	$676.57^{+87.97}_{-129.13}$	$3.15^{+2.87}_{-2.16}$	$46.61^{+0.04}_{-0.06}$
ω_0 ICs ($\zeta_0 = 0$)	$79.12^{+1.75}_{-1.73}$	$28.76^{+0.59}_{-0.6}$	$0.33^{+0.03}_{-0.02}$	$-0.19^{+0.05}_{-0.05}$	$0.24^{+0.03}_{-0.02}$	$\cdots$	$0.53^{+0.32}_{-0.32}$	$734.54^{+97.61}_{-147.69}$	$3.2^{+2.51}_{-2.52}$	$46.61^{+0.04}_{-0.06}$
$e_0 = 0$	$82.95^{+2.39}_{-2.54}$	$31.6^{+1.09}_{-0.94}$	$0.39^{+0.05}_{-0.04}$	$-0.17^{+0.06}_{-0.06}$	$\cdots$	$\cdots$	$0.53^{+0.32}_{-0.31}$	$874.23^{+125.43}_{-179.57}$	$3.11^{+2.55}_{-2.5}$	$43.38^{+0.04}_{-0.06}$

surrogate-waveform model. Regarding the instantaneous ICs, the quasicircular parameters are recovered with no biases, but a multimodal posterior in the eccentricity parameter is found in the middle panels of Fig. 7. These multimodalities can be explained by a degeneracy in the waveforms with fixed ζ_0 at a relatively high total mass ($M \sim 76 M_\odot$), and the fact that the model assumes circularization at merger-ringdown. As shown in Sec. III D these multimodalities can sometimes be an artifact of the specific parametrization chosen, and be removed by going to a definition of eccentricity based on the waveform. However, this is not the case for the injections shown in this section, and the multimodalities remain even after a redefinition of the eccentric parameters, indicating that for these particular injections these are true multimodalities in the posterior distribution. Therefore, the instantaneous ICs when neglecting ζ_0 can substantially complicate the sampling as well as the measurement of the eccentricity parameter due to the multimodalities.

Finally, we also show in Fig. 7 and Table II the results of sampling with the initial eccentricity set to zero. For the injection with small eccentricity at the injected SNR (~ 46) the quasicircular model is still able to recover the parameters accurately within the 90% credible intervals. However, for the high eccentricity injection ($e_0 = 0.2$) this is no longer the case and the biases in parameters like the chirp mass can be as large as 8% with respect to the injected value.

In summary, the orbit-averaged ICs provide a more efficient sampling of the eccentric parameter space than the instantaneous ones without a loss of accuracy. As a consequence we adopt the orbit-averaged ICs hereafter for the analysis using the SEOBNRv4EHM_opt model in this paper. Furthermore, we have shown that neglecting the radial-phase parameter, as currently done in the TEOBResumS-Dali and the SEOBNREHM [96] models can lead to biases in the recovered parameters for both instantaneous and orbit-averaged ICs, unless one varies additional parameters. For instance, in Ref. [85] to avoid biases in the posteriors with TEOBResumS-Dali, which only employs the eccentricity parameter to describe elliptical orbits, the starting frequency of the waveform is also sampled during the parameter estimation runs. However, we find more natural to keep the starting frequency of the waveform fixed as done in the LVK analysis of the Gravitational Wave Transient Catalogs [2–4], and thus, use two eccentric parameters, eccentricity and relativistic anomaly, which can vary freely during the parameter-estimation run.

D. Numerical-relativity injections

In Ref. [101], the SEOBNRv4EHM model was shown to be accurate to with an unfaithfulness below 1% for a dataset of public eccentric NR waveforms from the SXS catalog [106,177]. In this section we further investigate the accuracy of the SEOBNRv4EHM model against NR waveforms by performing zero-noise injections, and recovering the parameters with the SEOBNRv4E_opt model.

We consider a set of 3 public eccentric simulations SXS:BBH:1355, SXS:BBH:1359 and SXS:BBH:1363, which correspond to equal-mass, nonspinning configurations with initial eccentricities measured from the orbital frequency at first periastron passage of 0.07, 0.13 and 0.25, respectively (see Table I of Ref. [101] for details). For these injections we choose a total mass $M = 70 M_\odot$, inclination with respect to the line of sight of the BBH $\iota = 0$ rad, coalescence phase $\phi_{\rm ref} = 0$ rad, and luminosity distance $d_L = 2307$ Mpc, which produces a three-detector (LIGO Hanford, LIGO Livingston and Virgo) network-SNR of $\rho_{\rm mf}^N = 20$ when using the LIGO and Virgo PSD at design sensitivity. The priors are the same as in Sec. III C, with the only exception that for the run corresponding to the SXS:BBH:1363 NR waveform we set a larger upper bound for the eccentricity prior of $e_0 \in [0, 0.5]$ in order to avoid railing of the posterior against the upper bound of the prior.

Before analyzing the results of the injections, we consider the problem of mapping the eccentric parameters, eccentricity and radial phase, from the NR waveforms to the SEOBNRv4E_opt model. This problem stems from the gauge-dependency of the eccentricity parameter in general relativity, and can be avoided by adopting a common definition of the parameters defining elliptical orbits in the NR simulation and the SEOBNR model. In particular, we adopt a definition of eccentricity, $e_{\rm gw}$, measured from the frequency of the (2,2)-mode with the correct Newtonian limit [108]

$$e_{\rm gw} = \cos(\psi/3) - \sqrt{3} \sin(\psi/3), \tag{20a}$$

with

$$\psi = \arctan\left(\frac{1 - e_{\omega_{22}}^2}{2 e_{\omega_{22}}}\right), \tag{20b}$$

$$e_{\omega_{22}} = \frac{\omega_{22,p}^{1/2} - \omega_{22,a}^{1/2}}{\omega_{22,p}^{1/2} + \omega_{22,a}^{1/2}}, \tag{20c}$$

where $\omega_{22,a}$, $\omega_{22,p}$ refer to the values of the (2,2)-mode frequency at apastron and periastron, respectively. As the radial-phase parameter describing a binary in an elliptic orbit, we use the mean anomaly, with the following definition [178]

$$l_{\rm gw} = 2\pi \frac{t - t_i^p}{t_{i+1}^p - t_i^p}, \tag{21}$$

where t_i^p is the time of the ith periastron passage measured from the (2,2)-mode frequency.

These definitions of eccentricity and mean anomaly can be applied to the posterior distributions from the parameter-estimation runs as a post-processing step employing its highly efficient implementation in the GW_ECCENTRICITY
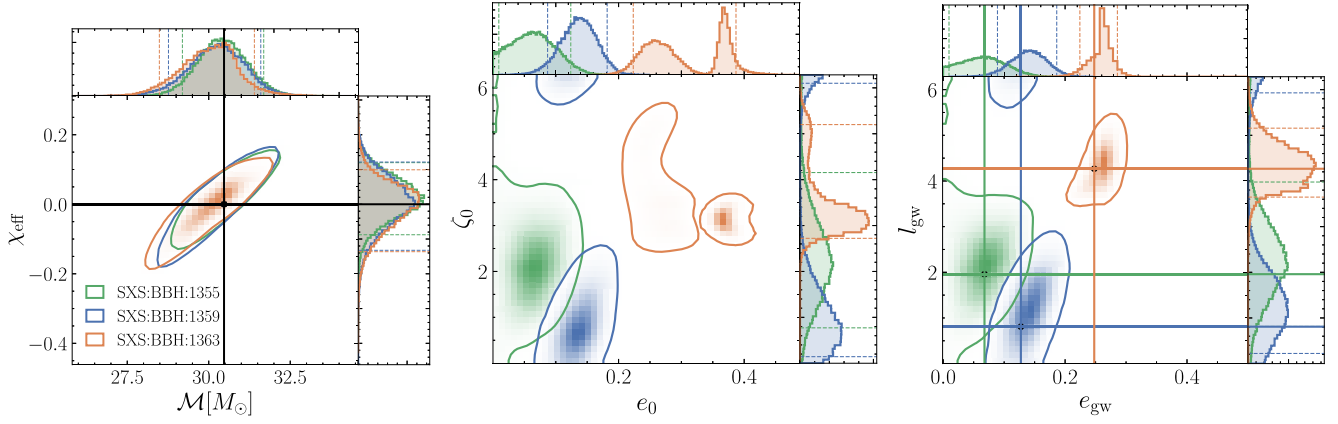
FIG. 8. 2D and 1D posterior distributions for some relevant parameters from the equal mass nonspinning synthetic BBH signals with total mass $70M_\odot$. The signal waveforms correspond to the NR waveforms from the public SXS catalog `SXS:BBH:1355`, `SXS:BBH:1359` and `SXS:BBH:1363` with GW eccentricities $e_{\rm gw} = 0.05, 0.1, 0.25$ and GW mean anomalies $l_{\rm gw} = 1.96, 0.81, 4.27$ defined at 20 Hz, respectively. The other parameters are specified in Table III. In the 2D posteriors the solid contours represent the 90% credible intervals and black dots show the values of the parameters of the injected signal. In the 1D posteriors they are represented by dashed and solid vertical lines, respectively. The parameter estimation is performed with the `SEOBNRv4E_opt` model. Left: chirp mass and effective-spin parameter. Middle: initial eccentricity and relativistic anomaly at 20 Hz. Right: GW eccentricity and GW mean anomaly at 20 Hz.

Python package[9] [109]. The procedure consists in evaluating the waveform for each sample of the posterior distributions, and applying the `GW_ECCENTRICITY` package to measure the eccentricity and mean anomaly at a desired point in the evolution. The process can be parallelized to measure the eccentricity and mean anomaly in a much smaller timescale than an actual parameter-estimation run.[10]

In the `SEOBNRv4EHM` model the eccentricity is specified at an orbit-averaged orbital frequency, however, the eccentricity definition introduced in Eq. (20) is based on the (2,2)-mode frequency. As shown in Ref. [108], for eccentric binaries the instantaneous orbital and (2,2)-mode frequencies are not related by a simple factor of 2, as in the quasicircular case, and this can cause that for some samples in the posterior distribution, the instantaneous (2,2)-mode frequency does not reach the starting frequency specified in the initial conditions of the `SEOBNRv4EHM` model. In order to avoid that this situation prevents the eccentricity measurement for some samples we have also implemented an option to integrate the EOB dynamics backward in time from a specific starting frequency. For the rest of the calculations involving `GW_ECCENTRICITY` in this paper, we integrate $2000M$ backward in time.

In Fig. 8, we summarize the parameter-estimation results of the injections. We report the marginalized 1D and 2D posteriors for the chirp mass $\mathcal{M}$ and the effective-spin parameter $\chi_{\rm eff}$, the initial eccentricity and relativistic

anomaly, and the GW eccentricity and mean anomaly measured at 20 Hz. In Table III we provide the values of the injected parameters and the median of the inferred posterior distribution with the 90% confidence intervals for both models. The results show that `SEOBNRv4E_opt` is able to recover $\mathcal{M}$ and $\chi_{\rm eff}$, as well as the mass ratio and total mass for all the NR injections within the 90% confidence intervals. The NR waveforms contain all the multipoles up to $l \le 8$, while the `SEOBNRv4E_opt` contains only the $(l, |m|) = (2, 2)$ modes. This difference in mode content explains why there are some small biases in the luminosity distance and $\theta_{\rm JN}$ parameter.

Regarding the eccentric parameters, the middle panel of Fig. 8 shows the initial eccentricity and relativistic anomaly posterior distributions at 20 Hz for the three different injections. For the highest eccentricity injection (`SXS:BBH:1363`), the eccentricity posterior is bimodal with two modes centered at $e_0 \sim 0.25$ and $e_0 \sim 0.35$. However, when moving to the definition of eccentricity and mean anomaly based on the (2,2)-mode frequency introduced in Eq. (20), we find a unimodal posterior in $e_{\rm gw}$ and $l_{\rm gw}$, which indicates that the bimodality in (e_0, l_0) is simply a consequence of the parametrization of the EOB initial conditions used in the `SEOBNRv4E_opt` model. Furthermore, the $e_{\rm gw}$ and $l_{\rm gw}$ parameters at 20 Hz are measured from the NR waveforms, and shown as vertical lines in the right panel of Fig. 8. The posterior distributions for $e_{\rm gw}$ and $l_{\rm gw}$ are consistent within the 90% credible intervals with the injected values for the three NR waveforms.

The results of the injections demonstrate that `SEOBNRv4E_opt` is able to accurately recover the eccentric and noneccentric parameters of the injected NR waveforms, and they are consistent with the low unfaithfulness

---

[9]We have used version `v1.0.2` from the public git repository `git@github.com:vijayvarma392/gw_eccentricity.git`.

[10]For the parameter-estimation runs in this section, and when running on 4 nodes of 32 cores (their description can be found in Sec. III C) the post-processing step takes less than 30 minutes.

TABLE III. Injected and median values of the posterior distributions for three synthetic NR injections with the same quasicircular parameters and different initial eccentricities, and recovered with `SEOBNRv4E_opt`. The median values also report the 90% credible intervals. The binary parameters correspond to the total mass M, chirp mass $\mathcal{M}$, inverse mass ratio $1/q$, effective-spin parameter χ_{eff}, initial eccentricity e_0, initial relativistic anomaly ζ_0, angle between the total angular momentum and the line of sight θ_{JN}, luminosity distance d_L, coalescence phase ϕ_{ref} and the network matched-filtered SNR for LIGO-Hanford/Livingston and Virgo detectors ρ_{mf}^N. At the bottom of the table the injected and measured GW eccentricity, e_{gw}, and GW mean anomaly, l_{gw}, are also reported.

Parameter	Injected value	SXS:1355	SXS:1359	SXS:1363
$M/M_\odot$	70.0	$70.87^{+2.47}_{-2.27}$	$70.41^{+2.45}_{-2.45}$	$69.81^{+2.32}_{-2.72}$
$\mathcal{M}/M_\odot$	30.47	$30.41^{+0.98}_{-0.95}$	$30.26^{+1.04}_{-1.14}$	$30.06^{+0.98}_{-1.21}$
$1/q$	1.0	$0.79^{+0.17}_{-0.19}$	$0.8^{+0.16}_{-0.19}$	$0.81^{+0.15}_{-0.17}$
χ_{eff}	0.0	$0.02^{+0.08}_{-0.08}$	$0.01^{+0.09}_{-0.1}$	$-0.0^{+0.08}_{-0.1}$
e_0	⋯	$0.06^{+0.05}_{-0.05}$	$0.14^{+0.03}_{-0.04}$	$0.29^{+0.09}_{-0.05}$
ζ_0	⋯	$2.23^{+1.37}_{-1.16}$	$1.01^{+4.67}_{-0.75}$	$3.28^{+1.6}_{-0.45}$
θ_{JN}	0.0	$0.62^{+0.48}_{-0.38}$	$0.61^{+0.48}_{-0.37}$	$0.61^{+0.47}_{-0.37}$
d_L	2307	1831^{+373}_{-560}	1818^{+374}_{-556}	1859^{+378}_{-571}
ϕ_{ref}	0.0	$3.15^{+2.5}_{-2.5}$	$3.14^{+2.51}_{-2.5}$	$3.16^{+2.52}_{-2.52}$
ρ_{mf}^N	20.0	$19.07^{+0.09}_{-0.14}$	$19.05^{+0.09}_{-0.15}$	$19.02^{+0.17}_{-0.15}$
e_{gw}	Injected	0.07	0.13	0.25
	Measured	$0.06^{+0.05}_{-0.05}$	$0.14^{+0.04}_{-0.03}$	$0.26^{+0.02}_{-0.03}$
l_{gw}	Injected	1.96	0.81	4.27
	Measured	$2.25^{+1.19}_{-1.11}$	$1.33^{+1.7}_{-0.93}$	$4.32^{+0.63}_{-0.54}$

values of `SEOBNRv4E` against NR waveforms reported in Ref. [101]. Further studies of the accuracy of the model will require larger datasets of eccentric NR waveforms including spins and higher eccentricities, and we leave for future work investigating the waveform systematics of the `SEOBNRv4EHM_opt` model and its biases against NR waveforms.

E. Analysis of GW events

In this section, we analyze 3 GW events recorded by the LIGO and Virgo detectors [1,3,4] during the first and third observing runs: GW150914, GW151226 and GW190521. We employ strain data from the Gravitational Wave Open Source Catalog (GWOSC) [179], and the released PSD and calibration envelopes included in the Gravitational Wave Transient Catalogs GWTC-2.1 [3], and their respective parameter-estimation samples releases.[11]

We analyze GW150914, GW151226 and GW190521 using `SEOBNRv4EHM_opt` and `SEOBNRv4E_opt` with

---

PARALLEL BILBY and the settings described in Sec. III A. For `SEOBNRv4EHM_opt`, we restrict to a mode content $l \leq 4$ in order to avoid the increase of computational cost due to the high sampling rates necessary to resolve the (5,5)-mode, as at the current SNRs the impact of this mode on accuracy is limited.

1. GW150914

The first observation of GWs from a BBH coalescence, GW150914, had one of the highest SNRs (∼23.7) of the GW events observed during the first three observing runs [3,110] of the LVK. The binary parameters are consistent with a nonspinning binary with comparable masses [114].

We choose priors in inverse mass ratio, $1/q \in [0.05, 1]$, and chirp mass, $\mathcal{M} \in [20, 50]M_\odot$, such that the induced priors in component masses are uniform. Uniform priors were also used for initial eccentricity, $e_0 \in [0, 0.3]$, and the initial relativistic anomaly, $\zeta_0 \in [0., 2\pi]$. The other priors are chosen as in Sec. III D. For the analysis we use a starting frequency of 10 Hz at which the waveform is generated and, thus at which the initial eccentricity and relativistic anomaly are defined. This choice of starting frequency ensures that the higher order modes in `SEOBNRv4EHM_opt` are in band at the minimum frequency of 20 Hz at which the likelihood calculation starts. We also remark the importance that both `SEOBNRv4EHM_opt` and `SEOBNRv4E_opt` are generated at the same starting frequency, so that both have the same priors in initial eccentricity.

The posterior distributions of chirp mass, effective-spin parameter, GW eccentricity and GW mean anomaly are displayed in the top row of Fig. 9. In Table IV we also report the median values and the 90% credible intervals of the posterior distributions for other binary parameters. For comparisons we include in our analysis the samples of `SEOBNRv4PHM` [168] from the GWTC-2.1 catalog [3]. We find that binary parameters like chirp mass, effective-spin parameter and mass ratio measured by `SEOBNRv4E_opt` and `SEOBNRv4EHM_opt` are consistent with the ones measured with `SEOBNRv4PHM`. This is expected as GW150914 is consistent with a nonspinning binary, and thus the effects of spin-precession which are accurately described by `SEOBNRv4PHM` are negligible. Regarding the eccentric parameters, although both `SEOBNRv4E_opt` and `SEOBNRv4EHM_opt` have median values of eccentricity distinct from zero, $e_{\mathrm{gw}}^{10\ \mathrm{Hz}} = 0.08^{+0.1}_{-0.07}$ and $e_{\mathrm{gw}}^{10\ \mathrm{Hz}} = 0.08^{+0.09}_{-0.06}$, respectively, the posterior distributions have a strong support in the zero eccentricity region, which is in agreement with other analyses of GW150914 with eccentric waveforms [73,85,86,114].[12] We also observe a
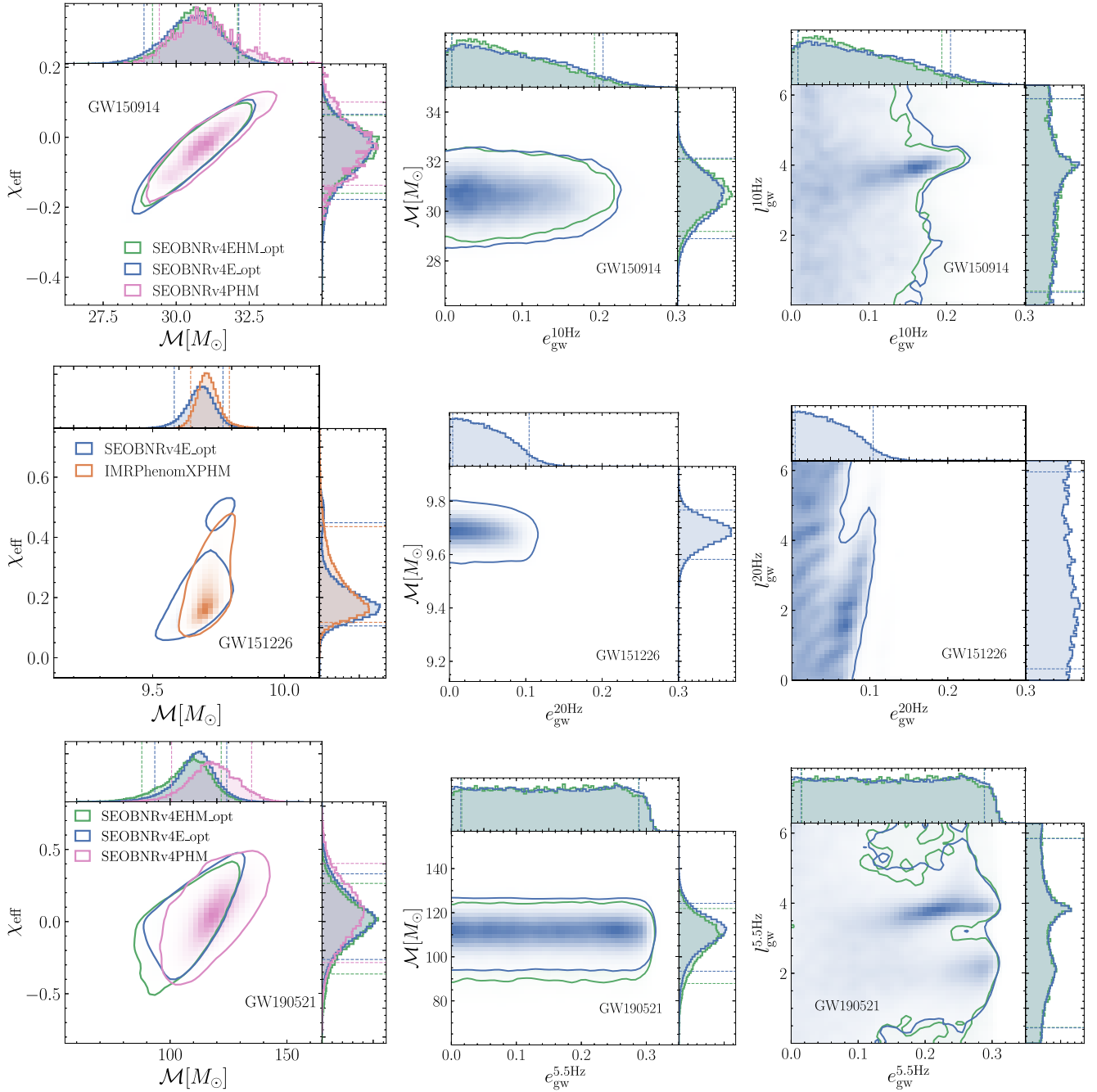

FIG. 9. Effective-spin parameter, chirp mass, GW eccentricity and GW mean anomaly parameters inferred for the real GW events analyzed with SEOBNRv4E_opt and SEOBNRv4EHM_opt. Comparisons are presented with the SEOBNRv4PHM (when available) and the IMRPhenomXPHM models from the GWTC-2.1 catalog [3], except for GW190521 where samples are from Refs. [112,113]. The waveform starting frequency for GW150914 is $f_{start} = 10$ Hz, for the low total mass event GW151226 is $f_{start} = 20$ Hz, in order to reduce the computational cost, while for GW190521 $f_{start} = 5.5$ Hz in order to have the mode content in band at the likelihood minimum frequency ($f_{min} = 11$ Hz).

small structure in the GW mean anomaly posterior, which is however not present in the relativistic anomaly posterior.[13] In order to better understand better this structure, we have

---

[13]For this event both the relativistic anomaly posteriors is uniform between $[0, 2\pi]$.

measured the eccentricity at different frequencies (12 and 13 Hz) and found that the small peak in the posteriors of GW mean anomaly is not present, while the posteriors in GW eccentricity remain qualitatively the same, except for the expected shift toward lower values due to the increase in frequency. This indicates that the minor structure in the GW

TABLE IV. Median and 90% credible intervals for the total mass, chirp mass, inverse mass ratio, effective-spin parameter, GW eccentricity, GW mean anomaly, $\theta_{\rm JN}$, luminosity distance and signal-versus-noise (natural) log Bayes factor, log $\mathcal{BF}$, measured with the SEOBNRv4E_opt and SEOBNRv4EHM_opt models for GW150914, GW151226 and GW190521. Additionally, we include the results of SEOBNRv4PHM for GW150914 and GW190521 and of IMRPhenomXPHM for GW151226 from the GWTC-2.1 catalog [3], except for GW190521 where samples are from Refs. [112,113]. The waveform starting frequency for GW150914 is $f_{\rm start} = 10$ Hz, for the low total mass event GW151226 is $f_{\rm start} = 20$ Hz, in order to reduce the computational cost, while for GW190521 is $f_{\rm start} = 5.5$ Hz in order to have the mode content in band at the likelihood minimum frequency ($f_{\rm min} = 11$ Hz).

Event	Waveform	$M/M_\odot$	$\mathcal{M}/M_\odot$	$1/q$	$\chi_{\rm eff}$	$e_{\rm gw}$	$l_{\rm gw}$	$\theta_{\rm JN}$	d_L	log $\mathcal{BF}$
GW150914 ($f_{\rm start} = 10$ Hz)	SEOBNRv4E_opt	$70.83^{+2.7}_{-2.88}$	$30.61^{+1.21}_{-1.32}$	$0.85^{+0.12}_{-0.16}$	$-0.04^{+0.08}_{-0.1}$	$0.08^{+0.1}_{-0.07}$	$3.31^{+2.2}_{-2.57}$	$2.48^{+0.4}_{-0.55}$	387^{+145}_{-133}	$283.9^{+0.1}_{-0.1}$
	SEOBNRv4EHM_opt	$70.89^{+2.42}_{-2.59}$	$30.72^{+1.08}_{-1.15}$	$0.89^{+0.09}_{-0.13}$	$-0.03^{+0.08}_{-0.09}$	$0.08^{+0.09}_{-0.06}$	$3.27^{+2.23}_{-2.49}$	$2.64^{+0.3}_{-0.37}$	440^{+117}_{-120}	$284.2^{+0.1}_{-0.1}$
	SEOBNRv4PHM	$71.32^{+3.39}_{-2.8}$	$30.92^{+1.51}_{-1.22}$	$0.9^{+0.08}_{-0.12}$	$-0.02^{+0.1}_{-0.09}$	⋯	⋯	$2.71^{+0.26}_{-0.59}$	492^{+103}_{-146}	⋯
GW151226 ($f_{\rm start} = 20$ Hz)	SEOBNRv4E_opt	$22.82^{+3.46}_{-0.59}$	$9.68^{+0.07}_{-0.07}$	$0.66^{+0.26}_{-0.32}$	$0.18^{+0.13}_{-0.06}$	$0.04^{+0.05}_{-0.04}$	$2.95^{+2.67}_{-2.3}$	$1.06^{+1.7}_{-0.73}$	468^{+170}_{-183}	$40.4^{+0.1}_{-0.1}$
	IMRPhenomXPHM	$23.71^{+6.13}_{-1.36}$	$9.71^{+0.06}_{-0.05}$	$0.52^{+0.35}_{-0.29}$	$0.2^{+0.17}_{-0.07}$	⋯	⋯	$0.87^{+1.94}_{-0.57}$	471^{+124}_{-154}	$47.6^{+0.1}_{-0.1}$
GW190521 ($f_{\rm start} = 5.5$ Hz)	SEOBNRv4E_opt	$259.92^{+21.63}_{-20.06}$	$111.15^{+9.88}_{-12.69}$	$0.74^{+0.2}_{-0.25}$	$0.02^{+0.23}_{-0.21}$	$0.15^{+0.12}_{-0.12}$	$3.14^{+2.26}_{-2.28}$	$1.27^{+1.43}_{-0.86}$	3924^{+1434}_{-1460}	$77.8^{+0.1}_{-0.1}$
	SEOBNRv4EHM_opt	$253.97^{+21.48}_{-24.94}$	$108.4^{+10.56}_{-15.27}$	$0.72^{+0.22}_{-0.24}$	$-0.01^{+0.21}_{-0.26}$	$0.15^{+0.12}_{-0.12}$	$3.16^{+2.25}_{-2.3}$	$0.88^{+1.89}_{-0.55}$	4172^{+1262}_{-1286}	$78.6^{+0.1}_{-0.1}$
	SEOBNRv4PHM	$279.54^{+36.74}_{-28.65}$	$118.13^{+12.94}_{-13.15}$	$0.74^{+0.2}_{-0.31}$	$0.06^{+0.26}_{-0.27}$	⋯	⋯	$1.39^{+1.28}_{-0.93}$	3964^{+1557}_{-1474}	⋯

mean anomaly posterior at 10 Hz is an artifact of the GW_ECCENTRICITY post-processing. We decide to keep the values at 10 Hz as this minor structure in GW mean anomaly does not change the overall conclusions, and with such reference frequency the eccentricity is measured at the same frequency as the rest of the binary parameters.

Additionally, we have produced a run with SEOBNRv4E_opt setting $e_0 = 0$, and obtained a signal-to-noise natural log Bayes factor of $284.6^{+0.1}_{-0.1}$ which is slightly larger than $283.9^{+0.1}_{-0.1}$ obtained for SEOBNRv4E_opt when sampling in (e_0, ζ_0) (see Table IV). Unfortunately, this information is not available for the SEOBNRv4PHM model in the public GWOSC results, but GWTC2-1 does include a log Bayes factor for the similar IMRPhenomXPHM model, of $\log \mathcal{BF} = 303.45^{+0.14}_{-0.14}$. These results indicate that the non-precessing eccentric hypothesis is disfavored against the precessing-spin quasicircular one, and that GW150914 is more consistent with a quasicircular BBH merger.

2. GW151226

GW151226 is one of the GW events with lowest total mass observed in the first observing run, and it was identified in the GWTC-1 catalog [1] to exclude support for $\chi_{\rm eff} = 0$ at $>90\%$ probability. Furthermore, Ref. [79] analyzed this event with the TEOBResumS-Dali model [175] and PARALLEL BILBY, with a uniform prior in eccentricity, and constrained the initial eccentricity to be $e_0 < 0.15$ at 90% at a starting frequency of 10 Hz. Moreover, Ref. [73] using the SEOBNRE model [95] and the reweighing technique with a log-uniform prior in eccentricity found a much tighter constraint $e_0 < 0.04$ at 10 Hz.

For our analysis we use a uniform prior in initial eccentricity $e_0 \in [0, 0.3]$ and relativistic anomaly $\zeta_0 \in [0, 2\pi]$, and priors in inverse mass ratio, $1/q \in [0.125, 1]$, and chirp mass, $\mathcal{M} \in [5, 100]M_\odot$, such that they are uniform in component masses. The rest of the priors are chosen as in the analysis of GW150914. We use a starting frequency of 20 Hz at which the waveform is generated and, at which e_0 and ζ_0 are defined. Due to the low total mass of the event, we restrict to a higher starting frequency than in the case of GW150914, and we only use the SEOBNRv4E_opt model in order to reduce the computational cost.

The results are shown in the middle row of Fig. 9, while in Table IV the median values and the 90% credible intervals of the posterior distributions are reported. For comparisons we include in our analysis the samples of IMRPhenomXPHM [180] from the GWTC-2.1 catalog [3]. The quasicircular binary parameters like chirp mass, effective-spin parameter and mass ratio measured by SEOBNRv4E_opt show differences with respect to the ones measured by IMRPhenomXPHM. This can be explained because of the different physical content of each model, as IMRPhenomXPHM includes higher-order modes and describes precessing-spin quasicircular binaries, while

`SEOBNRv4E_opt` includes only the $(l, |m|) = (2, 2)$ modes and describes nonprecessing eccentric binaries. This translates into a preference of `IMRPhenomXPHM` for unequal masses and larger effective spin values than `SEOBNRv4E_opt`. Apart from these differences, the posterior distributions of `SEOBNRv4E_opt` and `IMRPhenomXPHM` have large overlapping regions as can be observed in the left plot in the middle row of Fig. 9.

The value of eccentricity measured by `SEOBNRv4E_opt` is $e_{\rm gw}^{20\,\rm Hz} = 0.04^{+0.05}_{-0.04}$, and the posterior distribution of GW eccentricity (middle and right plots in Fig. 9) have strong support at zero eccentricity. This combined with an uninformative posterior distribution for the GW mean anomaly indicate that GW151226 is more consistent with a quasicircular binary than a nonprecessing eccentric binary with $e_0 \leq 0.3$. The comparison between the value of eccentricity in Table IV with the ones in Refs. [73,79] is challenging due to the following issues: the value of eccentricity that we report is computed at a different starting frequency (20 Hz), than the one (10 Hz) used in Refs. [73,79], and the definition of eccentricity that we are using is based on the waveforms generated from the samples, while Refs. [73,79] report the initial eccentricities considered in the definitions of the initial conditions in the `TEOBResumS-Dali` and `SEOBNRE` models. In order to estimate the eccentricity value at some other frequency we can apply the Newtonian relation between the eccentricity and frequency [23] $e = e_{\rm ref}(f/f_{\rm ref})^{-19/18}$ to our eccentricity measurement to obtain $e_{\rm gw}^{10\,\rm Hz} \sim 0.1$, which is closer to the value reported in Ref. [79]. This fact can be explained probably due to the fact that Ref. [73] uses a log-uniform prior in eccentricity which puts more weight on the low eccentricity region than a uniform prior.

Finally, we have also produced a run with `SEOBNRv4E_opt` setting $e_0 = 0$, and obtained a signal-to-noise natural log Bayes factor of $39.8^{+0.1}_{-0.1}$ which is slightly smaller than $40.4^{+0.1}_{-0.1}$ obtained for `SEOBNRv4E_opt` when sampling in (e_0, ζ_0) (see Table IV). The difference in log Bayes factors is ~ 0.6 which indicates a minor preference for the eccentric hypothesis. When comparing to the quasicircular precessing-spin results of `IMRPhenomXPHM` from the GWTC-2.1 catalog we find $\log \mathcal{BF} = 47.59^{+0.14}_{-0.14}$, which indicates that the eccentric nonprecessing spin hypothesis is less preferred than the precessing-spin quasicircular one with a log Bayes factors of ~ 7.2 in favor of the latter.

3. GW190521

GW190521 is particularly intriguing, with only 4 cycles in the band of the detectors, thus being consistent with a merger-ringdown dominated signal. It has been attributed to a variety of physical systems including a head-on collision of exotic compact objects [181], a nonspinning hyperbolic capture [82] and an eccentric binary [75,76], although some other recent studies do not find clear evidence for eccentricity [86].

We analyze GW190521 using the `SEOBNRv4EHM_opt` and `SEOBNRv4E_opt` models with a prior uniform in initial eccentricity, $e_0 \in [0, 0.3]$, and relativistic anomaly, $\zeta_0 \in [0, 2\pi]$. We employ priors in inverse mass ratio $1/q \in [0.05, 1]$, and chirp mass $\mathcal{M} \in [60, 200] M_\odot$ such that the induced priors are uniform in component masses. The rest of the priors are as in the analysis of GW150914, except for the luminosity distance prior which is chosen to be uniform in comoving volume instead of $\propto d_L^2$, in order to match the settings of Ref. [147]. The starting frequency of waveform generation is 5.5 Hz such that the higher-order modes are in band at the minimum frequency of the likelihood evaluation (11 Hz). As discussed in Ref. [182], the analysis of GW190521 using different sampling methods can lead to systematics in recovering some modes in the posterior distribution. In order to avoid that, we use a higher number of live points of 8192 for the PARALLEL BILBY runs of this event for `SEOBNRv4E_opt`, while for `SEOBNRv4EHM_opt` we use a lower number of live points 2048 to reduce the computational cost.[14]

The results of our analysis are shown in the bottom row of Fig. 9, while in Table IV the median values and the 90% credible intervals of the posterior distributions are reported. For comparisons we include in our analysis the samples of `SEOBNRv4PHM` from Refs. [112,113]. The quasicircular parameters like chirp mass or total mass show the largest differences with respect to the `SEOBNRv4PHM`, while other parameters like the effective-spin parameter and the mass ratio are quite consistent in the median. However, as in the case of nonprecessing quasicircular models (see Ref. [182]), the `SEOBNRv4EHM_opt` and `SEOBNRv4E_opt` models are not able to reproduce the secondary mode in the inverse mass ratio posterior. These differences between `SEOBNRv4PHM` and `SEOBNRv4EHM_opt` are expected due to the GW190521 signal being merger-ringdown dominated, and these waveform models include distinct physical effects.

Focusing on the eccentric parameters, we find median values of the GW eccentricity of $e_{\rm gw}^{5.5\,\rm Hz} = 0.15^{+0.12}_{-0.12}$ for both `SEOBNRv4EHM_opt` and `SEOBNRv4E_opt`. We observe a minor structure in the GW mean anomaly posterior, which can be explained by the same reasons as the ones discussed in the case of GW150914. The large median values of eccentricity contrast with the uninformative posterior distribution of eccentricity and the large uncertainty in the 90% credible intervals, which combined with an uninformative posterior distribution of the GW mean anomaly (see bottom panels of Fig. 9), indicates that the eccentricity parameter is poorly constrained in GW190521.

---

[14]We have also produced results for `SEOBNRv4E_opt` with a number of live points of 2048 and 4096, and observed only minimal differences in the posteriors with respect to the case with nlive = 8192. Therefore, for `SEOBNRv4EHM_opt`, we restricted to nlive = 2048 in order to reduce the computational cost of the run.

TABLE V. Settings and evaluation time for the different parameter estimation runs on real GW events. The mode content indicates the use of SEOBNRv4E_opt $[(2,|2|)]$ or SEOBNRv4EHM_opt (HMs $\equiv$ higher modes) to perform the run. Sampling rate (srate) and data segment duration (seglen) are specified in the data settings, while the number of autocorrelation times (nact) and number of live points (nlive) are specified in the sampler settings. The time reported is walltime, while the total computational cost in CPU hours can be obtained multiplying this time by the reported number of CPU cores employed.

GW event	Modes	Data settings		Sampler settings		Computing resources	
		srate (Hz)	seglen (s)	nact	nlive	cores × nodes	Runtime
GW150914 ($f_{start} = 10$ Hz)	$(2,|2|)$	4096	8	30	2048	32 × 10	6.7h
	HMs	4096	8	30	2048	32 × 10	3d 5h
GW151226 ($f_{start} = 20$ Hz)	$(2,|2|)$	4096	8	30	2048	32 × 16	1d 20h
GW190521 ($f_{start} = 5.5$ Hz)	$(2,|2|)$	4096	8	30	8192	32 × 10	1d 6h
	HMs	4096	8	30	2048	32 × 16	1d 5h

This situation can be explained by the fact that the signal is extremely short, and thus merger-ringdown dominated. However, in SEOBNRv4EHM_opt the eccentricity effects are included only through the inspiral-merger EOB modes, while at merger-ringdown the binary is assumed to have circularized, and the merger input values and the ringdown model are the same as in SEOBNRv4HM (see Sec. II for details). For moderate eccentricities, as the ones considered here, and nonprecessing spins it has been shown in Refs. [183–185] that the effects of eccentricity in the final mass and spin of NR waveforms are subdominant. However, nonprecessing large eccentricity, as well as precessing-spin eccentric cases are fairly unexplored. Therefore, in order to clearly measure eccentricity in high-mass systems, the binary should have large enough eccentricity at merger.

Apart from this limitation of the SEOBNRv4EHM_opt model,[15] we have also attempted to estimate the validity of the nonprecessing eccentric hypothesis versus the non-precessing quasicircular one by producing a run with SEOBNRv4E_opt setting $e_0 = 0$, and comparing the signal-to-noise Bayes factors. For the zero-eccentricity run with SEOBNRv4E_opt we find $\log \mathcal{BF} = 77.7^{+0.1}_{-0.1}$, which is consistent within the error bars with the values obtained for the eccentric run with SEOBNRv4E_opt, $\log \mathcal{BF} = 77.8^{+0.1}_{-0.1}$. This points out that the nonprecessing eccentric hypothesis is equally favored as the nonprecessing quasicircular one. However, when comparing to the quasicircular precessing-spin results from the discovery paper of GW190521[16] [112] we observe that for the NRSur7dq4 model [186] the log Bayes factor is $\log \mathcal{BF} = 84.49$. This produces a log Bayes factor between the quasicircular precessing-spin and nonprecessing eccentric hypothesis of ~ 6.7, indicating that the quasicircular

precessing-spin hypothesis is preferred over the nonprecessing eccentric one with a prior in $e_0 \in [0, 0.3]$.

The comparison of Bayes factors from different waveform models can be complicated as the result may be affected not only by the different physical effects included in the models, but also by the waveform systematics between the different waveform approximants. Different waveform models including the same physical effects can lead to different log Bayes factors (see for instance Table II of Ref. [182]). As a consequence, we consider the comparison of the eccentric nonprecessing against quasicircular precessing-spin hypothesis using log Bayes factors from other waveform families as an approximate estimate, and leave for future work a more detailed study [187].

Besides calibration to eccentric NR waveforms one of the main limitations in the analysis of GW190521 with SEOBNRv4EHM_opt is the lack of inclusion of spin-precession effects, which impact significantly the morphology of the templates at merger-ringdown, and may substantially modify the measured parameters. This points out the necessity to produce waveform models, which include both eccentricity and spin-precession effects, and there is ongoing work [188] to include both effects in the new generation of SEOBNR models [146,147] built within the new pySEOBNR python infrastructure [189].

Finally, the SEOBNRv4EHM_opt results have been obtained on the order of a few days or a week using PARALLEL BILBY (see Table V). This makes SEOBNRv4EHM_opt a standard tool that can be used with a highly parallelizable nested sampler like PARALLEL BILBY, and we plan to extend the Bayesian inference study presented here, using the machine-learning code DINGO [190–192], to all the GW events observed during the third-observing run [187].

IV. CONCLUSIONS

In this paper we have improved and validated the multipolar nonprecessing eccentric SEOBNRv4EHM model presented in Ref. [101], and shown its applicability to Bayesian inference studies.

---

[15]This is also the case of the other state-of-the-art inspiral-merger-ringdown eccentric waveform models, like TEOBResumS-Dali and SEOBNRE, used in other parameter estimation studies.

[16]We do not compare to the SEOBNRv4PHM results from GWTC-2.1, as the log Bayes factor is not provided with the public data.

The SEOBNRv4EHM model is built upon the quasicircular accurate NR-calibrated multipolar, nonprecessing SEOBNRv4HM model [102]. The eccentricity effects are included in the GW multipoles up to 2PN order including spin-orbit and spin-spin effects [100]. The multipolar SEOBNRv4EHM model includes the (2,2), (2,1), (3,3), (4,4), (5,5) modes, and it is shown in Ref. [101] to have an unfaithfulness against public eccentric NR waveforms below 1%.

Within the SEOBNRv4EHM model, elliptical orbits are described by two parameters, initial eccentricity, e_0, and initial relativistic anomaly, ζ_0, specified at an instantaneous orbital frequency ω_0. Here, we present a new parametrization of the initial conditions, where e_0 and ζ_0 are specified at an orbit-averaged orbital frequency $\bar{\omega}_0$. This new orbit-averaged initial conditions lead to smoother variations of e_0 and ζ_0 across parameter space, and as a consequence more efficient sampling of the parameter space.

The improvement in sampling efficiency due to the new initial conditions has also being accompanied with the development of SEOBNRv4EHM_opt, a faster version of the SEOBNRv4EHM model. The SEOBNRv4EHM_opt model combines a reduction of the absolute and relative tolerances of the Runge Kutta integrator from 10^{-10} and 10^{-9}, to 10^{-8} and 10^{-8}, with the use of the optimized Hamiltonian and integrator from Refs. [103,104]. These modifications lead to a factor of ~3–7 speed-up depending on the binary parameters. The reduction of the tolerances implies a reduction in accuracy of the SEOBNRv4EHM_opt model in the corners of parameter space (i.e., high eccentricities and high spins), where the model usage is limited, because it is very sensitive to the attachment point of the inspiral and merger-ringdown EOB modes. The trade-off between accuracy and efficiency of the new SEOBNRv4EHM_opt model, with a waveform evaluation time of $\mathcal{O}(100)$ ms, makes it a competitive model for use in parameter-estimation studies.

Given the accuracy and computational efficiency of SEOBNRv4EHM_opt, we have performed a Bayesian inference study on mock signals and real GW events detected by the LVK collaboration. We have first investigated the quasicircular limit of the SEOBNRv4EHM_opt model by computing the unfaithfulness against the quasicircular SEOBNRv4HM model [102] for 4500 random configurations in the parameter space $q \in [1, 50]$, spins $\chi_{1,2} \in [-0.9, 0.9]$ and total masses $M \in [20, 300]M_\odot$, at a dimensionless starting frequency of $M\omega = 0.023$. The results show that SEOBNRv4EHM_opt has a median unfaithfulness of 3.8×10^{-5} and no cases with unfaithfulness $> 1\%$, indicating that the quasicircular limit is accurately recovered. Furthermore, we have performed a mock-signal injection into zero noise using SEOBNRv4 [120] as a signal, and SEOBNRv4E_opt and SEOBNRv4_ROM [120] as templates. We have considered a configuration with mass ratio $q = 4$, total mass $M = 90.08M_\odot$ and BH's

dimensionless spins $\chi_1 = 0.5$ and $\chi_2 = -0.1$ defined at 20 Hz. The recovery of quasicircular parameters, like mass ratio, chirp mass or the effective-spin parameter by SEOBNRv4E_opt agrees remarkably well with the ones from SEOBNRv4_ROM. While the initial eccentricity and relativistic anomaly measured by SEOBNRv4E_opt are $e_0 = 0.01^{+0.02}_{-0.01}$ and $\zeta_0 = 3.09^{+2.57}_{-2.48}$, which indicate that the signal is compatible with zero eccentricity. Therefore, SEOBNRv4EHM_opt is able to correctly reproduce the zero-eccentricity limit, with an accuracy comparable to the underlying quasicircular model SEOBNRv4HM.

Moving to the eccentric sector, we have studied with zero-noise injections, using the SEOBNRv4E_opt as a signal and template, the impact of the initial conditions based on (e_0, ζ_0) specified at ω_0, and the new prescription, where (e_0, ζ_0) are specified at $\bar{\omega}_0$. For this study we have chosen a configuration with two different initial eccentricities $e_0 = [0.1, 0.2]$, mass ratio $q = 3$, initial relativistic anomaly $\zeta_0 = 1.2$, total mass $M = 76.4M_\odot$ and BH's dimensionless spins $\chi_1 = 0.5$ and $\chi_2 = -0.1$ defined at 20 Hz. The results show that both the orbit-averaged and the instantaneous initial conditions are able to accurately recover the corresponding injected signal, however, the averaged wall clock-time of the runs using the instantaneous initial conditions is a factor 3 slower than the orbit-averaged initial conditions, due to the complicated structure of the likelihood across the (e_0, ζ_0) parameter space in the case of the instantaneous initial conditions (see Fig. 2). As a consequence we adopt the orbit-averaged initial conditions as the default ones in the SEOBNRv4EHM and SEOBNRv4EHM_opt models.

Moreover, we have investigated the impact of neglecting the radial-phase parameter, relativistic anomaly, in the previous model injections by starting the orbits of the templates at periastron (i.e., $\zeta_0 = 0$). The posterior distributions of the orbit-averaged ICs show larger biases than the instantaneous ICs in the recovery of the quasicircular parameters, for instance, 8% bias in the case of the chirp mass, while in terms of the eccentricity parameter the instantaneous ICs may develop multimodalities in the posteriors, as is the case of the injections considered here, indicating that the parametrization cannot adequately reproduce the injected signal. For the orbit-averaged ICs the eccentricity parameter is compatible with the injected value within the 90% credible intervals. This indicates that neglecting the radial-phase parameter when performing parameter estimation of eccentric signals can induce biases not only in the measurement of the eccentricity, but also in the estimation of other quasicircular parameters like mass ratio or the spins due to the strong correlation of eccentricity with these parameters.

The accuracy of the SEOBNRv4EHM model in the eccentric case was investigated in Ref. [101] by computing the unfaithfulness of the model against a set of public eccentric NR waveforms from the SXS catalog [106,177].

Here we have also validated the accuracy of the `SEOBNRv4EHM_opt` model by performing a set of injections of synthetic NR signals into a network of LIGO-Virgo detectors at design sensitivity. We have injected into zero-detector noise three eccentric NR waveforms, `SXS:BBH:1355`, `SXS:BBH:1359` and `SXS:BBH:1363`, corresponding to equal-mass, nonspinning configurations with initial eccentricities measured from the orbital frequency at first periastron passage of 0.07, 0.13, and 0.25, respectively. For these injections we choose a total mass $M = 70M_\odot$, inclination $\iota = 0$ and SNR = 20. The results are summarized in Fig. 8 and Table III. In order to compare the eccentricity from the NR waveforms and the `SEOBNRv4EHM_opt` model, we have adopted a common definition of eccentricity and radial phase, based on the frequency of the (2,2)-mode [108], and used its efficient implementation in the open-source GW_ECCENTRICITY Python package [109] to postprocess the parameter estimation runs. We have found that the recovery of the parameters with `SEOBNRv4E_opt` does not produce significant biases, and that the measurement of the GW eccentricity, e_{gw}, and GW mean anomaly, l_{gw}, is consistent with the injected values for the three injections considered. A more comprehensive Bayesian inference study will be required to assess the modeling inaccuracies and how they translate into biases in both eccentric and quasicircular parameters. Here, new methods of inference such as machine learning techniques, like DINGO [190–192], may offer an alternative method to efficiently perform large-scale injections campaigns with moderate computational cost [187].

Besides injection studies, we have demonstrated that `SEOBNRv4EHM_opt` can be used as a standard tool in Bayesian inference studies of real GW events. We have analyzed three GW events (GW150914, GW151226 and GW190521) detected by the LVK Collaboration in the first and third observing runs. The eccentricity measured for the three events is $e_{gw,\,10\,Hz}^{GW150914} = 0.08_{-0.06}^{+0.09}$, $e_{gw,\,20\,Hz}^{GW151226} = 0.04_{-0.04}^{+0.05}$, and $e_{gw,\,5.5\,Hz}^{GW190521} = 0.15_{-0.12}^{+0.12}$. As a consequence, we do not find clear evidence of orbital eccentricity in any of the GW events considered, when using a nonprecessing eccentric model with initial eccentricities $e_0 \in [0, 0.3]$. For the GW150914 and GW151226 we have compared with the quasicircular results from the GWTC-2.1 catalog [3], while for GW190521 with the results from Refs. [112,113] (the precessing-spin `SEOBNRv4PHM` [168] and `IMRPhenomXPHM` [180] models). For GW150914 we find good agreement with `SEOBNRv4PHM` due to the fact that the event is consistent with a nonspinning binary, while for GW151226 and GW190521, we find some discrepancies, which are likely due to the inclusion of spin-precession effects in the quasicircular models, which are not included in the `SEOBNRv4EHM_opt` model. This is a clear limitation of the `SEOBNRv4EHM_opt` model as well as all the

current existing inspiral-merger-ringdown eccentric waveform models. There is ongoing work [188] to include such effects in the new generation of `SEOBNR` models [146,147] developed within the new `pySEOBNR` infrastructure [189].

Regarding the analysis of real GW events, we plan in the future to extend the Bayesian inference study presented here, using the machine-learning code DINGO, to all the GW events detected during the third-observing run [187] in order to set constraints on the eccentricity of the observed population of BBHs.

APPENDIX: DERIVATION OF THE ORBIT-AVERAGED ORBITAL FREQUENCY

The initial conditions for eccentric orbits were derived in Sec. II C of Ref. [101], given an initial (instantaneous)

orbital frequency ω, eccentricity e, and relativistic anomaly ζ. In order to perform orbital evolutions starting from different points on (roughly) the same eccentric orbit, we derive an expression for the instantaneous frequency in terms of the orbit-averaged frequency.

We use the Keplerian parametrization

$$r = \frac{1}{u_p(1 + e \cos \zeta)}, \tag{A1}$$

and perform the following steps, in a PN expansion up to 2PN order:

(1) Calculate the orbit-averaged azimuthal frequency

$$\bar{\omega} \equiv \frac{1}{T_r} \oint \dot{\phi} dt = \frac{1}{T_r} \oint \frac{\partial H}{\partial p_\phi} \left(\frac{\partial H}{\partial p_r} \right)^{-1} dr$$

$$= \frac{2}{T_r} \int_0^\pi \frac{\partial H}{\partial p_\phi} \left(\frac{\partial H}{\partial p_r} \right)^{-1} \frac{dr}{d\zeta} d\zeta, \tag{A2}$$

where T_r is the radial period, and is given by

$$T_r \equiv \oint dt = 2 \int_0^\pi \left(\frac{\partial H}{\partial p_r} \right)^{-1} \frac{dr}{d\zeta} d\zeta, \tag{A3}$$

yielding

$$\bar{\omega} = (u_p - e^2 u_p)^{3/2} \left\{ 1 + \frac{u_p}{2c^2} [\nu - e^2(\nu - 6)] + \frac{u_p^{3/2}}{2c^3} (3e^2 + 1)[(\nu - 2)\chi_S - 2\delta\chi_A] \right.$$

$$+ \frac{3u_p^2}{8c^4} \left[e^4(\nu^2 - 5\nu + 24) - 2e^2 \left(4\nu\sqrt{1 - e^2} - 10\sqrt{1 - e^2} + \nu^2 + \nu + 3 \right) \right.$$

$$\left. + 8\sqrt{1 - e^2}\nu - 20\sqrt{1 - e^2} + \nu^2 - 13\nu + 20 \right] - \frac{3u_p^2}{2c^4} [2\delta\chi_A\chi_S[e^2(\nu - 1) - \nu]$$

$$\left. + e^2(4\nu - 1)\chi_A^2 + [2(\nu - 1)\nu - e^2(2\nu^2 - 2\nu + 1)]\chi_S^2] \right\} + \mathcal{O}(1/c^5), \tag{A4}$$

where the powers of $1/c$ indicate the PN order of the different terms.

(2) Invert $\bar{\omega}(u_p, e)$ to obtain $u_p(\bar{\omega}, e)$, i.e. the inverse semilatus rectum as a function of the averaged frequency, which at leading order is given by

$$u_p(\bar{\omega}, e) = \frac{\bar{\omega}^{2/3}}{1 - e^2} + \frac{\bar{\omega}^{4/3}(e^2(\nu - 6) - \nu)}{3c^2(e^2 - 1)^2} + \frac{(3e^2 + 1)\bar{\omega}^{5/3}(2\delta\chi_A - (\nu - 2)\chi_S)}{3c^3(1 - e^2)^{5/2}}$$

$$+ \frac{\bar{\omega}^2}{4c^4(e^2 - 1)^3} \left\{ -2e^2 \left[\nu \left(4\delta\chi_A\chi_S + 8\chi_A^2 + 4\sqrt{1 - e^2} + 4\chi_S^2 + 7 \right) - 4\delta\chi_A\chi_S \right.\right.$$

$$\left. - 2\chi_A^2 - 10\sqrt{1 - e^2} - 4\nu^2\chi_S^2 - 2\chi_S^2 + 3 \right] + \nu \left(8\delta\chi_A\chi_S + 8\sqrt{1 - e^2} + 8\chi_S^2 - 13 \right)$$

$$\left. + e^4(7\nu - 12) - 20 \left(\sqrt{1 - e^2} - 1 \right) - 8\nu^2\chi_S^2 \right\} + \mathcal{O}(1/c^5). \tag{A5}$$

(3) Calculate the instantaneous orbital frequency (in Keplerian parametrization)

$$\omega(u_p, e, \zeta) = \frac{\partial H}{\partial p_\phi} = u_p^{3/2}(e \cos \zeta + 1)^2 - \frac{u_p^{5/2}}{2c^2} (e \cos \zeta + 1)^2 [(e^2 - 1)\nu + 4e \cos \zeta]$$

$$- \frac{u_p^3}{2c^3} (e^2 - 2e \cos \zeta + 1)(e \cos \zeta + 1)^2 (2\delta\chi_A - (\nu - 2)\chi_S)$$

$$+ \frac{u_p^{7/2}}{8c^4} (e \cos \zeta + 1)^2 \{ -16e^2\nu\chi_A^2 + 8e \cos \zeta [\nu(8\delta\chi_A\chi_S + 8\chi_A^2 + e^2 + 8\chi_S^2 - 1)$$

$$- 2(2\delta\chi_A\chi_S + \chi_A^2 + \chi_S^2 + 2) - 8\nu^2\chi_S^2] + 4e^2 \cos 2\zeta [(4\nu - 1)\chi_A^2 + 2\delta(2\nu - 1)\chi_A\chi_S - (1 - 2\nu)^2\chi_S^2]$$

$$- 8\delta e^2\nu\chi_A\chi_S + 8\delta e^2\chi_A\chi_S + 4e^2\chi_A^2 + 24\delta\nu\chi_A\chi_S + 3e^4\nu^2 - 3e^4\nu - 6e^2\nu^2 + 2e^2\nu + 8e^2\nu^2\chi_S^2 - 8e^2\nu\chi_S^2$$

$$+ 4e^2\chi_S^2 + 16e^2 + 3\nu^2 - 15\nu - 24\nu^2\chi_S^2 + 24\nu\chi_S^2 \} + \mathcal{O}(1/c^5). \tag{A6}$$

(4) Plug $u_p(\bar{\omega}, e)$ in $\omega(u_p, e, \zeta)$ to obtain $\omega(\bar{\omega}, e, \zeta)$, which reads

$$
\begin{aligned}
\omega = {} & \frac{\bar{\omega}(e\cos\zeta+1)^2}{(1-e^2)^{3/2}} - \frac{e\bar{\omega}^{5/3}(3e+2\cos\zeta)(e\cos\zeta+1)^2}{c^2(1-e^2)^{5/2}} - \frac{e\bar{\omega}^2(e+\cos\zeta)}{c^3(e^2-1)^3}(1+e\cos\zeta)^2[2\delta\chi_A - (\nu-2)\chi_S] \\
& - \frac{\bar{\omega}^{7/3}(e\cos\zeta+1)^2}{12c^4(1-e^2)^{7/2}}\Big\{ 12e^4(\nu-6) + 8e(e^2(\nu-15)-\nu+6)\cos\zeta - 3e^2\Big[2\Big(6\sqrt{1-e^2}+7\Big)\nu - 30\sqrt{1-e^2}+17\Big] \\
& + 18\Big(\sqrt{1-e^2}-1\Big)(2\nu-5)\Big\} + \frac{e\bar{\omega}^{7/3}(e\cos\zeta+1)^2}{2c^4(1-e^2)^{7/2}}\{2\delta\chi_A\chi_S[e(2\nu-1)\cos(2\zeta)+2e(\nu-1)+(8\nu-4)\cos\zeta] \\
& + \chi_S^2[-e(4\nu^2+(1-2\nu)^2\cos(2\zeta)-4\nu+2)-4(1-2\nu)^2\cos\zeta] + (4\nu-1)\chi_A^2[e(\cos(2\zeta)+2)+4\cos\zeta]\} + \mathcal{O}(1/c^5).
\end{aligned}
\tag{A7}
$$

Thus, we start with a given initial orbit-averaged frequency $\bar{\omega}$, eccentricity e, and relativistic anomaly ζ. Then, use Eq. (A7) to compute the instantaneous frequency $\omega(\bar{\omega}, e, \zeta)$, and follow the same procedure as in Ref. [101] to obtain the initial conditions for the dynamical variables.

---

[1] B. P. Abbott *et al.* (LIGO Scientific and Virgo Collaborations), GWTC-1: A gravitational-wave transient catalog of compact binary mergers observed by LIGO and Virgo during the first and second observing runs, Phys. Rev. X **9**, 031040 (2019).

[2] R. Abbott *et al.* (LIGO Scientific and Virgo Collaborations), GWTC-2: Compact binary coalescences observed by LIGO and Virgo during the first half of the third observing run, Phys. Rev. X **11**, 021053 (2021).

[3] R. Abbott *et al.* (LIGO Scientific and Virgo Collaborations), GWTC-2.1: Deep extended catalog of compact binary coalescences observed by LIGO and Virgo during the first half of the third observing run, arXiv:2108.01045 [Phys. Rev. D (to be published)].

[4] R. Abbott *et al.* (LIGO Scientific, VIRGO, and KAGRA Collaborations), GWTC-3: Compact binary coalescences observed by LIGO and Virgo during the second part of the third observing run, Phys. Rev. X **13**, 041039 (2023).

[5] Alexander H. Nitz, Collin D. Capano, Sumit Kumar, Yi-Fan Wang, Shilpa Kastha, Marlin Schäfer, Rahul Dhurkunde, and Miriam Cabero, 3-OGC: Catalog of gravitational waves from compact-binary mergers, Astrophys. J. **922**, 76 (2021).

[6] Seth Olsen, Tejaswi Venumadhav, Jonathan Mushkin, Javier Roulet, Barak Zackay, and Matias Zaldarriaga, New binary black hole mergers in the LIGO-Virgo O3a data, Phys. Rev. D **106**, 043009 (2022).

[7] T. Akutsu *et al.* (KAGRA Collaboration), KAGRA: 2.5 generation interferometric gravitational wave detector, Nat. Astron. **3**, 35 (2019).

[8] T. Akutsu *et al.* (KAGRA Collaboration), Overview of KAGRA: Detector design and construction history, Prog. Theor. Exp. Phys. **2021**, 05A101 (2021).

[9] Hans A. Bethe and G. E. Brown, Evolution of binary compact objects which merge, Astrophys. J. **506**, 780 (1998).

[10] Krzysztof Belczynski, Vassiliki Kalogera, and Tomasz Bulik, A comprehensive study of binary compact objects as gravitational wave sources: Evolutionary channels, rates, and physical properties, Astrophys. J. **572**, 407 (2001).

[11] Michal Dominik, Krzysztof Belczynski, Christopher Fryer, Daniel E. Holz, Emanuele Berti, Tomasz Bulik, Ilya Mandel, and Richard O'Shaughnessy, Double compact objects II: Cosmological merger rates, Astrophys. J. **779**, 72 (2013).

[12] Krzysztof Belczynski, Alessandra Buonanno, Matteo Cantiello, Chris L. Fryer, Daniel E. Holz, Ilya Mandel, M. Coleman Miller, and Marek Walczak, The formation and gravitational-wave detection of massive stellar black-hole binaries, Astrophys. J. **789**, 120 (2014).

[13] Nicki Mennekens and Dany Vanbeveren, Massive double compact object mergers: Gravitational wave sources and r-process element production sites, Astron. Astrophys. **564**, A134 (2014).

[14] Mario Spera, Michela Mapelli, and Alessandro Bressan, The mass spectrum of compact remnants from the parsec stellar evolution tracks, Mon. Not. R. Astron. Soc. **451**, 4086 (2015).

[15] Krzysztof Belczynski, Daniel E. Holz, Tomasz Bulik, and Richard O'Shaughnessy, The first gravitational-wave source from the isolated evolution of two 40-100 Msun stars, Nature (London) **534**, 512 (2016).

[16] J. J. Eldridge and E. R. Stanway, BPASS predictions for binary black-hole mergers, Mon. Not. R. Astron. Soc. **462**, 3302 (2016).

[17] Pablo Marchant, Norbert Langer, Philipp Podsiadlowski, Thomas M. Tauris, and Takashi J. Moriya, A new route towards merging massive black holes, Astron. Astrophys. **588,** A50 (2016).

[18] Michela Mapelli, Nicola Giacobbo, Emanuele Ripamonti, and Mario Spera, The cosmic merger rate of stellar black hole binaries from the Illustris simulation, Mon. Not. R. Astron. Soc. **472,** 2422 (2017).

[19] Michela Mapelli and Nicola Giacobbo, The cosmic merger rate of neutron stars and black holes, Mon. Not. R. Astron. Soc. **479,** 4391 (2018).

[20] Simon Stevenson, Alejandro Vigna-Gómez, Ilya Mandel, Jim W. Barrett, Coenraad J. Neijssel, David Perkins, and Selma E. de Mink, Formation of the first three gravitational-wave observations through isolated binary evolution, Nat. Commun. **8,** 14906 (2017).

[21] Nicola Giacobbo and Michela Mapelli, The progenitors of compact-object binaries: Impact of metallicity, common envelope and natal kicks, Mon. Not. R. Astron. Soc. **480,** 2011 (2018).

[22] Matthias U. Kruckow, Thomas M. Tauris, Norbert Langer, Michael Kramer, and Robert G. Izzard, Progenitors of gravitational wave mergers: Binary evolution with the stellar grid-based code ComBinE, Mon. Not. R. Astron. Soc. **481,** 1908 (2018).

[23] P. C. Peters, Gravitational radiation and the motion of two point masses, Phys. Rev. **136,** B1224 (1964).

[24] Simon F. Portegies Zwart and Stephen McMillan, Black hole mergers in the universe, Astrophys. J. Lett. **528,** L17 (2000).

[25] M. Coleman Miller and Douglas P. Hamilton, Production of intermediate-mass black holes in globular clusters, Mon. Not. R. Astron. Soc. **330,** 232 (2002).

[26] M. Coleman Miller and Douglas P. Hamilton, Four-body effects in globular cluster black hole coalescence, Astrophys. J. **576,** 894 (2002).

[27] Kayhan Gultekin, M. Coleman Miller, and Douglas P. Hamilton, Growth of intermediate-mass black holes in globular clusters, Astrophys. J. **616,** 221 (2004).

[28] Kayhan Gultekin, M. Coleman Miller, and Douglas P. Hamilton, Three-body dynamics with gravitational wave emission, Astrophys. J. **640,** 156 (2006).

[29] Ryan M. O'Leary, Frederic A. Rasio, John M. Fregeau, Natalia Ivanova, and Richard W. O'Shaughnessy, Binary mergers and growth of black holes in dense star clusters, Astrophys. J. **637,** 937 (2006).

[30] Aleksander Sadowski, Krzysztof Belczynski, Tomasz Bulik, Natalia Ivanova, Frederic A. Rasio, and Richard W. O'Shaughnessy, The total merger rate of compact object binaries in the local universe, Astrophys. J. **676,** 1162 (2008).

[31] J. M. B. Downing, M. J. Benacquista, M. Giersz, and R. Spurzem, Compact binaries in star clusters–I. Black hole binaries inside globular clusters, Mon. Not. R. Astron. Soc. **407,** 1946 (2010).

[32] J. M. B. Downing, M. J. Benacquista, M. Giersz, and R. Spurzem, Compact binaries in star clusters–II. Escapers and detection rates, Mon. Not. R. Astron. Soc. **416,** 133 (2011).

[33] Johan Samsing, Morgan MacLeod, and Enrico Ramirez-Ruiz, The formation of eccentric compact binary inspirals and the role of gravitational wave emission in binary-single stellar encounters, Astrophys. J. **784,** 71 (2014).

[34] Carl L. Rodriguez, Meagan Morscher, Bharath Pattabiraman, Sourav Chatterjee, Carl-Johan Haster, and Frederic A. Rasio, Binary black hole mergers from globular clusters: Implications for Advanced LIGO, Phys. Rev. Lett. **115,** 051101 (2015); **116,** 029901(E) (2016).

[35] Abbas Askar, Magdalena Szkudlarek, Dorota Gondek-Rosińska, Mirek Giersz, and Tomasz Bulik, Mocca-Survey database—I. Coalescing binary black holes originating from globular clusters, Mon. Not. R. Astron. Soc. **464,** L36 (2017).

[36] Carl L. Rodriguez, Sourav Chatterjee, and Frederic A. Rasio, Binary black hole mergers from globular clusters: Masses, merger rates, and the impact of stellar evolution, Phys. Rev. D **93,** 084029 (2016).

[37] Carl L. Rodriguez, Carl-Johan Haster, Sourav Chatterjee, Vicky Kalogera, and Frederic A. Rasio, Dynamical formation of the GW150914 binary black hole, Astrophys. J. Lett. **824,** L8 (2016).

[38] Johan Samsing and Enrico Ramirez-Ruiz, On the assembly rate of highly eccentric binary black hole mergers, Astrophys. J. Lett. **840,** L14 (2017).

[39] Johan Samsing, Eccentric black hole mergers forming in globular clusters, Phys. Rev. D **97,** 103014 (2018).

[40] Carl L. Rodriguez, Pau Amaro-Seoane, Sourav Chatterjee, and Frederic A. Rasio, Post-Newtonian dynamics in dense star clusters: Highly-eccentric, highly-spinning, and repeated binary black hole mergers, Phys. Rev. Lett. **120,** 151101 (2018).

[41] Carl L. Rodriguez and Abraham Loeb, Redshift evolution of the black hole merger rate from globular clusters, Astrophys. J. Lett. **866,** L5 (2018).

[42] Giacomo Fragione and Bence Kocsis, Black hole mergers from an evolving population of globular clusters, Phys. Rev. Lett. **121,** 161103 (2018).

[43] Michael Zevin, Johan Samsing, Carl Rodriguez, Carl-Johan Haster, and Enrico Ramirez-Ruiz, Eccentric black hole mergers in dense star clusters: The role of binary–binary encounters, Astrophys. J. **871,** 91 (2019).

[44] László Gondán and Bence Kocsis, High eccentricities and high masses characterize gravitational-wave captures in galactic nuclei as seen by earth-based detectors, Mon. Not. R. Astron. Soc. **506,** 1665 (2021).

[45] Ryan M. O'Leary, Bence Kocsis, and Abraham Loeb, Gravitational waves from scattering of stellar-mass black holes in galactic nuclei, Mon. Not. R. Astron. Soc. **395,** 2127 (2009).

[46] Fabio Antonini and Hagai B. Perets, Secular evolution of compact binaries near massive black holes: Gravitational wave sources and other exotica, Astrophys. J. **757,** 27 (2012).

[47] David Tsang, Shattering flares during close encounters of neutron stars, Astrophys. J. **777,** 103 (2013).

[48] Fabio Antonini and Frederic A. Rasio, Merging black hole binaries in galactic nuclei: Implications for Advanced-LIGO detections, Astrophys. J. **831,** 187 (2016).

[49] Cristobal Petrovich and Fabio Antonini, Greatly enhanced merger rates of compact-object binaries in nonspherical nuclear star clusters, Astrophys. J. **846,** 146 (2017).

[50] Nicholas C. Stone, Brian D. Metzger, and Zoltán Haiman, Assisted inspirals of stellar mass black holes embedded in AGN discs: Solving the 'final au problem', Mon. Not. R. Astron. Soc. **464,** 946 (2017).

[51] Nicholas C. Stone, Andreas H. W. Küpper, and Jeremiah P. Ostriker, Formation of massive black holes in galactic nuclei: Runaway tidal encounters, Mon. Not. R. Astron. Soc. **467,** 4180 (2017).

[52] Alexander Rasskazov and Bence Kocsis, The rate of stellar mass black hole scattering in galactic nuclei, Astrophys. J. **881,** 20 (2019).

[53] Ilya Mandel and Richard O'Shaughnessy, Compact binary coalescences in the band of ground-based gravitational-wave detectors, Classical Quantum Gravity **27,** 114007 (2010).

[54] B. P. Abbott et al. (LIGO Scientific and Virgo Collaborations), Astrophysical implications of the binary black-hole merger GW150914, Astrophys. J. Lett. **818,** L22 (2016).

[55] Will M. Farr, Simon Stevenson, M. Coleman Miller, Ilya Mandel, Ben Farr, and Alberto Vecchio, Distinguishing spin-aligned and isotropic black hole populations with gravitational waves, Nature (London) **548,** 426 (2017).

[56] B. P. Abbott et al. (LIGO Scientific and Virgo Collaborations), Binary black hole population properties inferred from the first and second observing runs of Advanced LIGO and Advanced Virgo, Astrophys. J. Lett. **882,** L24 (2019).

[57] Michael Zevin, Isobel M. Romero-Shaw, Kyle Kremer, Eric Thrane, and Paul D. Lasky, Implications of eccentric observations on binary black hole formation channels, Astrophys. J. Lett. **921,** L43 (2021).

[58] R. Abbott et al. (The LIGO Scientific Collaboration, the Virgo Collaboration, and the KAGRA Collaboration), The population of merging compact binaries inferred using gravitational waves through GWTC-3, Phys. Rev. X **13,** 011048 (2023).

[59] A. G. Abac et al. (LIGO Scientific, VIRGO, and KAGRA Collaborations), Search for eccentric black hole coalescences during the third observing run of LIGO and Virgo, arXiv:2308.03822.

[60] B. P. Abbott et al. (KAGRA, LIGO Scientific, Virgo, VIRGO), Prospects for observing and localizing gravitational-wave transients with Advanced LIGO, Advanced Virgo and KAGRA, Living Rev. Relativity **21,** 3 (2018).

[61] Peter Fritschel, Stuart Reid, Gabriele Vajente, Giles Hammond, Haixing Miao, Daniel Brown, Volker Quetschke, and Jessica Steinlechner, Instrument science white paper 2021, Report No. LIGO-T2100298, 2021, https://dcc.ligo.org/LIGO-T2100298/public.

[62] The Virgo Collaboration, Advanced Virgo technical design report, Report No. VIR-0128A-12, 2012.

[63] M. Punturo et al., The Einstein telescope: A third-generation gravitational wave observatory, Classical Quantum Gravity **27,** 194002 (2010).

[64] Benjamin P. Abbott et al. (LIGO Scientific Collaboration), Exploring the sensitivity of next generation gravitational

wave detectors, Classical Quantum Gravity **34,** 044001 (2017).

[65] David Reitze et al., The US program in ground-based gravitational wave science: Contribution from the LIGO laboratory, Bull. Am. Astron. Soc. **51,** 141 (2019).

[66] David Reitze et al., Cosmic explorer: The U.S. contribution to gravitational-wave astronomy beyond LIGO, Bull. Am. Astron. Soc. **51,** 035 (2019).

[67] Pau Amaro-Seoane et al., Laser interferometer space antenna, arXiv:1702.00786.

[68] Jun Luo et al. (TianQin Collaboration), TianQin: A space-borne gravitational wave detector, Classical Quantum Gravity **33,** 035010 (2016).

[69] Alberto Sesana, Self consistent model for the evolution of eccentric massive black hole binaries in stellar environments: Implications for gravitational wave observations, Astrophys. J. **719,** 851 (2010).

[70] Katelyn Breivik, Carl L. Rodriguez, Shane L. Larson, Vassiliki Kalogera, and Frederic A. Rasio, Distinguishing between formation channels for binary black holes with LISA, Astrophys. J. Lett. **830,** L18 (2016).

[71] Johan Samsing and Daniel J. D'Orazio, Black hole mergers from globular clusters observable by LISA I: Eccentric sources originating from relativistic N-body dynamics, Mon. Not. R. Astron. Soc. **481,** 5445 (2018).

[72] Vitor Cardoso, Caio F. B. Macedo, and Rodrigo Vicente, Eccentricity evolution of compact binaries and applications to gravitational-wave physics, Phys. Rev. D **103,** 023015 (2021).

[73] Isobel M. Romero-Shaw, Paul D. Lasky, and Eric Thrane, Searching for eccentricity: Signatures of dynamical formation in the first gravitational-wave transient catalogue of LIGO and Virgo, Mon. Not. R. Astron. Soc. **490,** 5210 (2019).

[74] Alexander H. Nitz, Amber Lenon, and Duncan A. Brown, Search for eccentric binary neutron star mergers in the first and second observing runs of Advanced LIGO, Astrophys. J. **890,** 1 (2019).

[75] Isobel M. Romero-Shaw, Paul D. Lasky, Eric Thrane, and Juan Calderon Bustillo, GW190521: Orbital eccentricity and signatures of dynamical formation in a binary black hole merger signal, Astrophys. J. Lett. **903,** L5 (2020).

[76] V. Gayathri, J. Healy, J. Lange, B. O'Brien, M. Szczepanczyk, I. Bartos, M. Campanelli, S. Klimenko, C. Lousto, and R. O'Shaughnessy, GW190521 as a highly eccentric black hole merger, Nat. Astron. **6,** 344 (2022).

[77] Shichao Wu, Zhoujian Cao, and Zong-Hong Zhu, Measuring the eccentricity of binary black holes in GWTC-1 by using the inspiral-only waveform, Mon. Not. R. Astron. Soc. **495,** 466 (2020).

[78] Marc Favata, Chunglee Kim, K. G. Arun, JeongCho Kim, and Hyung Won Lee, Constraining the orbital eccentricity of inspiralling compact binary systems with Advanced LIGO, Phys. Rev. D **105,** 023003 (2022).

[79] Eamonn O'Shea and Prayush Kumar, Correlations in parameter estimation of low-mass eccentric binaries: GW151226 & GW170608, Phys. Rev. D **108,** 104018 (2023).

[80] Isobel M. Romero-Shaw, Davide Gerosa, and Nicholas Loutrel, Eccentricity or spin precession? Distinguishing

subdominant effects in gravitational-wave data, Mon. Not. R. Astron. Soc. **519,** 5352 (2023).

[81] Isobel M. Romero-Shaw, Paul D. Lasky, and Eric Thrane, Signs of eccentricity in two gravitational-wave signals may indicate a sub-population of dynamically assembled binary black holes, arXiv:2108.01284.

[82] Rossella Gamba, Matteo Breschi, Gregorio Carullo, Simone Albanesi, Piero Rettegno, Sebastiano Bernuzzi, and Alessandro Nagar, GW190521 as a dynamical capture of two nonspinning black holes, Nat. Astron. **7,** 11 (2023).

[83] Isobel M. Romero-Shaw, Paul D. Lasky, and Eric Thrane, Four eccentric mergers increase the evidence that LIGO–Virgo–KAGRA's binary black holes form dynamically, Astrophys. J. **940,** 171 (2022).

[84] Alan M. Knee, Isobel M. Romero-Shaw, Paul D. Lasky, Jess McIver, and Eric Thrane, A Rosetta stone for eccentric gravitational waveform models, Astrophys. J. **936,** 172 (2022).

[85] Alice Bonino, Rossella Gamba, Patricia Schmidt, Alessandro Nagar, Geraint Pratten, Matteo Breschi, Piero Rettegno, and Sebastiano Bernuzzi, Inferring eccentricity evolution from observations of coalescing binary black holes, Phys. Rev. D **107,** 064024 (2023).

[86] H. L. Iglesias *et al.*, Reassessing candidate eccentric binary black holes: Results with a model including higher-order modes, arXiv:2208.01766.

[87] Divyajyoti, Sumit Kumar, Snehal Tibrewal, Isobel M. Romero-Shaw, and Chandra Kant Mishra, Blind spots and biases: The dangers of ignoring eccentricity in gravitational-wave signals from binary black holes, arXiv:2309.16638.

[88] Xiaolin Liu, Zhoujian Cao, and Zong-Hong Zhu, Effective-one-body numerical-relativity waveform model for eccentric spin-precessing binary black hole coalescence, arXiv:2310.04552.

[89] A. Buonanno and T. Damour, Effective one-body approach to general relativistic two-body dynamics, Phys. Rev. D **59,** 084006 (1999).

[90] Alessandra Buonanno and Thibault Damour, Transition from inspiral to plunge in binary black hole coalescences, Phys. Rev. D **62,** 064015 (2000).

[91] Thibault Damour, Piotr Jaranowski, and Gerhard Schaefer, On the determination of the last stable orbit for circular general relativistic binaries at the third post-Newtonian approximation, Phys. Rev. D **62,** 084011 (2000).

[92] Thibault Damour, Coalescence of two spinning black holes: An effective one-body approach, Phys. Rev. D **64,** 124013 (2001).

[93] Alessandra Buonanno, Yanbei Chen, and Thibault Damour, Transition from inspiral to plunge in precessing binaries of spinning black holes, Phys. Rev. D **74,** 104005 (2006).

[94] Andrea Taracchini, Yi Pan, Alessandra Buonanno, Enrico Barausse, Michael Boyle, Tony Chu, Geoffrey Lovelace, Harald P. Pfeiffer, and Mark A. Scheel, Prototype effective-one-body model for nonprecessing spinning inspiral-merger-ringdown waveforms, Phys. Rev. D **86,** 024011 (2012).

[95] Zhoujian Cao and Wen-Biao Han, Waveform model for an eccentric binary black hole based on the effective-one-body-numerical-relativity formalism, Phys. Rev. D **96,** 044028 (2017).

[96] Xiaolin Liu, Zhoujian Cao, and Zong-Hong Zhu, A higher-multipole gravitational waveform model for an eccentric binary black holes based on the effective-one-body-numerical-relativity formalism, Classical Quantum Gravity **39,** 035009 (2022).

[97] Teagan A. Clarke, Isobel M. Romero-Shaw, Paul D. Lasky, and Eric Thrane, Gravitational-wave inference for eccentric binaries: The argument of periapsis, Mon. Not. R. Astron. Soc. **517,** 3778 (2022).

[98] Danilo Chiaramello and Alessandro Nagar, Faithful analytical effective-one-body waveform model for spin-aligned, moderately eccentric, coalescing black hole binaries, Phys. Rev. D **101,** 101501 (2020).

[99] Alessandro Nagar, Alice Bonino, and Piero Rettegno, Effective one-body multipolar waveform model for spin-aligned, quasicircular, eccentric, hyperbolic black hole binaries, Phys. Rev. D **103,** 104021 (2021).

[100] Mohammed Khalil, Alessandra Buonanno, Jan Steinhoff, and Justin Vines, Radiation-reaction force and multipolar waveforms for eccentric, spin-aligned binaries in the effective-one-body formalism, Phys. Rev. D **104,** 024046 (2021).

[101] Antoni Ramos-Buades, Alessandra Buonanno, Mohammed Khalil, and Serguei Ossokine, Effective-one-body multipolar waveforms for eccentric binary black holes with nonprecessing spins, Phys. Rev. D **105,** 044035 (2022).

[102] Roberto Cotesta, Alessandra Buonanno, Alejandro Bohé, Andrea Taracchini, Ian Hinder, and Serguei Ossokine, Enriching the symphony of gravitational waves from binary black holes by tuning higher harmonics, Phys. Rev. D **98,** 084028 (2018).

[103] Caleb Devine, Zachariah B. Etienne, and Sean T. McWilliams, Optimizing spinning time-domain gravitational waveforms for Advanced LIGO data analysis, Classical Quantum Gravity **33,** 125025 (2016).

[104] Tyler D. Knowles, Caleb Devine, David A. Buch, Serdar A. Bilgili, Thomas R. Adams, Zachariah B. Etienne, and Sean T. Mcwilliams, Improving performance of SEOBNRv3 by ∼300x, Classical Quantum Gravity **35,** 155003 (2018).

[105] Rory J. E. Smith, Gregory Ashton, Avi Vajpeyi, and Colm Talbot, Massively parallel Bayesian inference for transient gravitational-wave astronomy, Mon. Not. R. Astron. Soc. **498,** 4492 (2020).

[106] Michael Boyle *et al.*, The SXS Collaboration catalog of binary black hole simulations, Classical Quantum Gravity **36,** 195006 (2019).

[107] Tanja Hinderer and Stanislav Babak, Foundations of an effective-one-body model for coalescing binaries on eccentric orbits, Phys. Rev. D **96,** 104048 (2017).

[108] Antoni Ramos-Buades, Maarten van de Meent, Harald P. Pfeiffer, Hannes R. Rüter, Mark A. Scheel, Michael Boyle, and Lawrence E. Kidder, Eccentric binary black holes: Comparing numerical relativity and small mass-ratio perturbation theory, Phys. Rev. D **106,** 124040 (2022).

[109] Md Arif Shaikh, Vijay Varma, Harald P. Pfeiffer, Antoni Ramos-Buades, and Maarten van de Meent, Defining eccentricity for gravitational wave astronomy, Phys. Rev. D **108,** 104007 (2023).

[110] B. P. Abbott et al. (LIGO Scientific and Virgo Collaborations), Observation of gravitational waves from a binary black hole merger, Phys. Rev. Lett. **116,** 061102 (2016).

[111] B. P. Abbott et al. (LIGO Scientific and Virgo Collaborations), GW151226: Observation of gravitational waves from a 22-solar-mass binary black hole coalescence, Phys. Rev. Lett. **116,** 241103 (2016).

[112] R. Abbott et al. (LIGO Scientific and Virgo Collaborations), GW190521: A binary black hole merger with a total mass of $150M_\odot$, Phys. Rev. Lett. **125,** 101102 (2020).

[113] R. Abbott et al. (LIGO Scientific and Virgo Collaborations), Properties and astrophysical implications of the $150M_\odot$ binary black hole merger GW190521, Astrophys. J. Lett. **900,** L13 (2020).

[114] Benjamin P. Abbott et al. (LIGO Scientific and Virgo Collaborations), Effects of waveform model systematics on the interpretation of GW150914, Classical Quantum Gravity **34,** 104002 (2017).

[115] B. S. Sathyaprakash and B. F. Schutz, Physics, astrophysics and cosmology with gravitational waves, Living Rev. Relativity **12,** 2 (2009).

[116] Etienne Racine, Analysis of spin precession in binary black hole systems including quadrupole-monopole interaction, Phys. Rev. D **78,** 044021 (2008).

[117] L. Santamaria et al., Matching post-Newtonian and numerical relativity waveforms: Systematic errors and a new phenomenological model for nonprecessing black hole binaries, Phys. Rev. D **82,** 064016 (2010).

[118] Enrico Barausse and Alessandra Buonanno, Extending the effective-one-body Hamiltonian of black-hole binaries to include next-to-next-to-leading spin-orbit couplings, Phys. Rev. D **84,** 104027 (2011).

[119] Andrea Taracchini et al., Effective-one-body model for black-hole binaries with generic mass ratios and spins, Phys. Rev. D **89,** 061502 (2014).

[120] Alejandro Bohé et al., Improved effective-one-body model of spinning, nonprecessing binary black holes for the era of gravitational-wave astrophysics with advanced detectors, Phys. Rev. D **95,** 044028 (2017).

[121] Yi Pan, Alessandra Buonanno, Michael Boyle, Luisa T. Buchman, Lawrence E. Kidder, Harald P. Pfeiffer, and Mark A. Scheel, Inspiral-merger-ringdown multipolar waveforms of nonspinning black-hole binaries using the effective-one-body formalism, Phys. Rev. D **84,** 124052 (2011).

[122] Yi Pan, Alessandra Buonanno, Andrea Taracchini, Lawrence E. Kidder, Abdul H. Mroué, Harald P. Pfeiffer, Mark A. Scheel, and Béla Szilágyi, Inspiral-merger-ringdown waveforms of spinning, precessing black-hole binaries in the effective-one-body formalism, Phys. Rev. D **89,** 084006 (2014).

[123] Thibault Damour, Bala R. Iyer, and Alessandro Nagar, Improved resummation of post-Newtonian multipolar waveforms from circularized compact binaries, Phys. Rev. D **79,** 064004 (2009).

[124] Yi Pan, Alessandra Buonanno, Ryuichi Fujita, Etienne Racine, and Hideyuki Tagoshi, Post-Newtonian factorized multipolar waveforms for spinning, non-precessing black-hole binaries, Phys. Rev. D **83,** 064003 (2011); **87,** 109901 (E) (2013).

[125] A. Gopakumar and Bala R. Iyer, Gravitational waves from inspiralling compact binaries: Angular momentum flux, evolution of the orbital elements and the wave form to the second post-Newtonian order, Phys. Rev. D **56,** 7708 (1997).

[126] A. Gopakumar and Bala R. Iyer, Second post-Newtonian gravitational wave polarizations for compact binaries in elliptical orbits, Phys. Rev. D **65,** 084011 (2002).

[127] Thibault Damour, Achamveedu Gopakumar, and Bala R. Iyer, Phasing of gravitational waves from inspiralling eccentric binaries, Phys. Rev. D **70,** 064028 (2004).

[128] Christian Konigsdorffer and Achamveedu Gopakumar, Phasing of gravitational waves from inspiralling eccentric binaries at the third-and-a-half post-Newtonian order, Phys. Rev. D **73,** 124012 (2006).

[129] K. G. Arun, Luc Blanchet, Bala R. Iyer, and Moh'd S. S. Qusailah, Tail effects in the 3PN gravitational wave energy flux of compact binaries in quasi-elliptical orbits, Phys. Rev. D **77,** 064034 (2008).

[130] K. G. Arun, Luc Blanchet, Bala R. Iyer, and Moh'd S. S. Qusailah, Inspiralling compact binaries in quasi-elliptical orbits: The complete 3PN energy flux, Phys. Rev. D **77,** 064035 (2008).

[131] K. G. Arun, Luc Blanchet, Bala R. Iyer, and Siddhartha Sinha, Third post-Newtonian angular momentum flux and the secular evolution of orbital elements for inspiralling compact binaries in quasi-elliptical orbits, Phys. Rev. D **80,** 124018 (2009).

[132] Raoul-Martin Memmesheimer, Achamveedu Gopakumar, and Gerhard Schaefer, Third post-Newtonian accurate generalized quasi-Keplerian parametrization for compact binaries in eccentric orbits, Phys. Rev. D **70,** 104011 (2004).

[133] Nicolas Yunes, K. G. Arun, Emanuele Berti, and Clifford M. Will, Post-circular expansion of eccentric binary inspirals: Fourier-domain waveforms in the stationary phase approximation, Phys. Rev. D **80,** 084001 (2009); **89,** 109901(E) (2014).

[134] E. A. Huerta, Prayush Kumar, Sean T. McWilliams, Richard O'Shaughnessy, and Nicolás Yunes, Accurate and efficient waveforms for compact binaries on eccentric orbits, Phys. Rev. D **90,** 084016 (2014).

[135] Chandra Kant Mishra, K. G. Arun, and Bala R. Iyer, Third post-Newtonian gravitational waveforms for compact binary systems in general orbits: Instantaneous terms, Phys. Rev. D **91,** 084040 (2015).

[136] Nicholas Loutrel and Nicolás Yunes, Eccentric gravitational wave bursts in the post-Newtonian formalism, Classical Quantum Gravity **34,** 135011 (2017).

[137] Antoine Klein, Yannick Boetzel, Achamveedu Gopakumar, Philippe Jetzer, and Lorenzo de Vittori, Fourier domain gravitational waveforms for precessing eccentric binaries, Phys. Rev. D **98,** 104043 (2018).

[138] Blake Moore, Travis Robson, Nicholas Loutrel, and Nicolas Yunes, Towards a Fourier domain waveform for non-spinning binaries with arbitrary eccentricity, Classical Quantum Gravity **35,** 235006 (2018).

[139] Blake Moore and Nicolás Yunes, A 3PN Fourier domain waveform for non-spinning binaries with moderate eccentricity, Classical Quantum Gravity **36,** 185003 (2019).

[140] Sashwat Tanay, Antoine Klein, Emanuele Berti, and Atsushi Nishizawa, Convergence of Fourier-domain templates for inspiraling eccentric compact binaries, Phys. Rev. D **100,** 064006 (2019).

[141] Srishti Tiwari and Achamveedu Gopakumar, Combining post-circular and Padé approximations to compute Fourier domain templates for eccentric inspirals, Phys. Rev. D **102,** 084042 (2020).

[142] Gregory Ashton et al., BILBY: A user-friendly Bayesian inference library for gravitational-wave astronomy, Astrophys. J. Suppl. Ser. **241,** 27 (2019).

[143] I. M. Romero-Shaw et al., Bayesian inference for compact binary coalescences with bilby: Validation and application to the first LIGO–Virgo gravitational-wave transient catalogue, Mon. Not. R. Astron. Soc. **499,** 3295 (2020).

[144] Mohammed Khalil, Alessandra Buonanno, Héctor Estellés, Deyan P. Mihaylov, Serguei Ossokine, Lorenzo Pompili, and Antoni Ramos-Buades, Theoretical groundwork supporting the precessing-spin two-body dynamics of the effective-one-body waveform models SEOBNRv5, arXiv:2303.18143.

[145] Deyan P. Mihaylov, Serguei Ossokine, Alessandra Buonanno, Hector Estelles, Lorenzo Pompili, Michael Pürrer, and Antoni Ramos-Buades, pySEOBNR: A software package for the next generation of effective-one-body multipolar waveform models, arXiv:2303.18203.

[146] Lorenzo Pompili et al., Laying the foundation of the effective-one-body waveform models SEOBNRv5: Improved accuracy and efficiency for spinning non-precessing binary black holes, arXiv:2303.18039.

[147] Antoni Ramos-Buades, Alessandra Buonanno, Héctor Estellés, Mohammed Khalil, Deyan P. Mihaylov, Serguei Ossokine, Lorenzo Pompili, and Mahlet Shiferaw, SEOBNRv5PHM: Next generation of accurate and efficient multipolar precessing-spin effective-one-body waveforms for binary black holes, arXiv:2303.18046.

[148] Maarten van de Meent, Alessandra Buonanno, Deyan P. Mihaylov, Serguei Ossokine, Lorenzo Pompili, Niels Warburton, Adam Pound, Barry Wardell, Leanne Durkan, and Jeremy Miller, Enhancing the SEOBNRv5 effective-one-body waveform model with second-order gravitational self-force fluxes, arXiv:2303.18026.

[149] Scott E. Field, Chad R. Galley, Jan S. Hesthaven, Jason Kaye, and Manuel Tiglio, Fast prediction and evaluation of gravitational waveforms using surrogate models, Phys. Rev. X **4,** 031006 (2014).

[150] Michael Pürrer, Frequency domain reduced order models for gravitational waves from aligned-spin compact binaries, Classical Quantum Gravity **31,** 195010 (2014).

[151] Michael Pürrer, Frequency domain reduced order model of aligned-spin effective-one-body waveforms with generic mass-ratios and spins, arXiv:1512.02248.

[152] Benjamin D. Lackey, Sebastiano Bernuzzi, Chad R. Galley, Jeroen Meidam, and Chris Van Den Broeck, Effective-one-body waveforms for binary neutron stars using surrogate models, Phys. Rev. D **95,** 104036 (2017).

[153] Benjamin D. Lackey, Michael Pürrer, Andrea Taracchini, and Sylvain Marsat, Surrogate model for an aligned-spin effective one body waveform model of binary neutron star inspirals using Gaussian process regression, Phys. Rev. D **100,** 024002 (2019).

[154] Roberto Cotesta, Sylvain Marsat, and Michael Pürrer, Frequency domain reduced order model of aligned-spin effective-one-body waveforms with higher-order modes, Phys. Rev. D **101,** 124040 (2020).

[155] Bhooshan Gadre, Michael Pürrer, Scott E. Field, Serguei Ossokine, and Vijay Varma, A fully precessing higher-mode surrogate model of effective-one-body waveforms, arXiv:2203.00381.

[156] Sebastian Khan and Rhys Green, Gravitational-wave surrogate models powered by artificial neural networks, Phys. Rev. D **103,** 064015 (2021).

[157] Lucy M. Thomas, Geraint Pratten, and Patricia Schmidt, Accelerating multimodal gravitational waveforms from precessing compact binaries with artificial neural networks, Phys. Rev. D **106,** 104029 (2022).

[158] Alessandro Nagar and Piero Rettegno, Efficient effective one body time-domain gravitational waveforms, Phys. Rev. D **99,** 021501 (2019).

[159] Deyan P. Mihaylov, Serguei Ossokine, Alessandra Buonanno, and Abhirup Ghosh, Fast post-adiabatic waveforms in the time domain: Applications to compact binary coalescences in LIGO and Virgo, Phys. Rev. D **104,** 124087 (2021).

[160] Priscilla Canizares, Scott E. Field, Jonathan Gair, Vivien Raymond, Rory Smith, and Manuel Tiglio, Accelerated gravitational-wave parameter estimation with reduced order modeling, Phys. Rev. Lett. **114,** 071104 (2015).

[161] Rory Smith, Scott E. Field, Kent Blackburn, Carl-Johan Haster, Michael Pürrer, Vivien Raymond, and Patricia Schmidt, Fast and accurate inference on gravitational waves from precessing compact binaries, Phys. Rev. D **94,** 044031 (2016).

[162] Soichiro Morisaki and Vivien Raymond, Rapid parameter estimation of gravitational waves from binary neutron star coalescence using focused reduced order quadrature, Phys. Rev. D **102,** 104020 (2020).

[163] Jacopo Tissino, Gregorio Carullo, Matteo Breschi, Rossella Gamba, Stefano Schmidt, and Sebastiano Bernuzzi, Combining effective-one-body accuracy and reduced-order-quadrature speed for binary neutron star merger parameter estimation with machine learning, Phys. Rev. D **107,** 084037 (2023).

[164] Barak Zackay, Liang Dai, and Tejaswi Venumadhav, Relative binning and fast likelihood evaluation for gravitational wave parameter estimation, arXiv:1806.08792.

[165] B. S. Sathyaprakash and S. V. Dhurandhar, Choice of filters for the detection of gravitational waves from coalescing binaries, Phys. Rev. D **44,** 3819 (1991).

[166] Lee Samuel Finn and David F. Chernoff, Observing binary inspiral in gravitational radiation: One interferometer, Phys. Rev. D **47,** 2198 (1993).

[167] Lisa Barsotti, Peter Fritschel, Matthew Evans, and Slawomir Gras (LIGO Collaboration), Updated Advanced LIGO sensitivity design curve, LIGO Document No. T1800044-v5, 2018.

[168] Serguei Ossokine *et al.*, Multipolar effective-one-body waveforms for precessing binary black holes: Construction and validation, Phys. Rev. D **102,** 044055 (2020).

[169] Joshua S. Speagle, DYNESTY: A dynamic nested sampling package for estimating Bayesian posteriors and evidences, Mon. Not. R. Astron. Soc. **493,** 3132 (2020).

[170] J. Veitch *et al.*, Parameter estimation for compact binaries with ground-based gravitational-wave observations using the LALInference software library, Phys. Rev. D **91,** 042003 (2015).

[171] Tyson B. Littenberg, John G. Baker, Alessandra Buonanno, and Bernard J. Kelly, Systematic biases in parameter estimation of binary black-hole mergers, Phys. Rev. D **87,** 104003 (2013).

[172] Vijay Varma, Parameswaran Ajith, Sascha Husa, Juan Calderon Bustillo, Mark Hannam, and Michael Pürrer, Gravitational-wave observations of binary black holes: Effect of nonquadrupole modes, Phys. Rev. D **90,** 124004 (2014).

[173] N. V. Krishnendu and Frank Ohme, Interplay of spin-precession and higher harmonics in the parameter estimation of binary black holes, Phys. Rev. D **105,** 064012 (2022).

[174] Alessandro Nagar *et al.*, Time-domain effective-one-body gravitational waveforms for coalescing compact binaries with nonprecessing spins, tides and self-spin effects, Phys. Rev. D **98,** 104052 (2018).

[175] Alessandro Nagar and Piero Rettegno, Next generation: Impact of high-order analytical information on effective one body waveform models for noncircularized, spin-aligned black hole binaries, Phys. Rev. D **104,** 104004 (2021).

[176] Tousif Islam, Vijay Varma, Jackie Lodman, Scott E. Field, Gaurav Khanna, Mark A. Scheel, Harald P. Pfeiffer, Davide Gerosa, and Lawrence E. Kidder, Eccentric binary black hole surrogate models for the gravitational waveform and remnant properties: comparable mass, nonspinning case, Phys. Rev. D **103,** 064022 (2021).

[177] Ian Hinder, Lawrence E. Kidder, and Harald P. Pfeiffer, Eccentric binary black hole inspiral-merger-ringdown gravitational waveform model from numerical relativity and post-Newtonian theory, Phys. Rev. D **98,** 044015 (2018).

[178] Patricia Schmidt, Ian W. Harry, and Harald P. Pfeiffer, Numerical relativity injection infrastructure, arXiv:1703.01076.

[179] Rich Abbott *et al.* (LIGO Scientific and Virgo Collaborations), Open data from the first and second observing runs of Advanced LIGO and Advanced Virgo, SoftwareX **13,** 100658 (2021).

[180] Geraint Pratten *et al.*, Computationally efficient models for the dominant and subdominant harmonic modes of precessing binary black holes, Phys. Rev. D **103,** 104056 (2021).

[181] Juan Calderón Bustillo, Nicolas Sanchis-Gual, Alejandro Torres-Forné, José A. Font, Avi Vajpeyi, Rory Smith, Carlos Herdeiro, Eugen Radu, and Samson H. W. Leong, GW190521 as a merger of proca stars: A potential new vector boson of 8.7×10^{-13} eV, Phys. Rev. Lett. **126,** 081101 (2021).

[182] Héctor Estellés *et al.*, A detailed analysis of GW190521 with phenomenological waveform models, Astrophys. J. **924,** 79 (2022).

[183] Ian Hinder, Birjoo Vaishnav, Frank Herrmann, Deirdre Shoemaker, and Pablo Laguna, Universality and final spin in eccentric binary black hole inspirals, Phys. Rev. D **77,** 081502 (2008).

[184] E. A. Huerta *et al.*, Physics of eccentric binary black hole mergers: A numerical relativity perspective, Phys. Rev. D **100,** 064003 (2019).

[185] Antoni Ramos-Buades, Sascha Husa, Geraint Pratten, Héctor Estellés, Cecilio García-Quirós, Maite Mateu-Lucena, Marta Colleoni, and Rafel Jaume, First survey of spinning eccentric black hole mergers: Numerical relativity simulations, hybrid waveforms, and parameter estimation, Phys. Rev. D **101,** 083015 (2020).

[186] Vijay Varma, Scott E. Field, Mark A. Scheel, Jonathan Blackman, Davide Gerosa, Leo C. Stein, Lawrence E. Kidder, and Harald P. Pfeiffer, Surrogate models for precessing binary black hole simulations with unequal masses, Phys. Rev. Res. **1,** 033015 (2019).

[187] Nihar Gupte *et al.* (to be published).

[188] Aldo Gamboa *et al.* (to be published).

[189] Deyan P. Mihaylov, Serguei Ossokine, Alessandra Buonanno, Hector Estelles, Lorenzo Pompili, Michael Pürrer, and Antoni Ramos-Buades, pySEOBNR: A software package for the next generation of effective-one-body multipolar waveform models, arXiv:2303.18203.

[190] Stephen R. Green and Jonathan Gair, Complete parameter inference for GW150914 using deep learning, Mach. Learn. Sci. Tech. **2,** 03LT01 (2021).

[191] Maximilian Dax, Stephen R. Green, Jonathan Gair, Jakob H. Macke, Alessandra Buonanno, and Bernhard Schölkopf, Real-time gravitational wave science with neural posterior estimation, Phys. Rev. Lett. **127,** 241103 (2021).

[192] Maximilian Dax, Stephen R. Green, Jonathan Gair, Michael Pürrer, Jonas Wildberger, Jakob H. Macke, Alessandra Buonanno, and Bernhard Schölkopf, Neural importance sampling for rapid and reliable gravitational-wave inference, Phys. Rev. Lett. **130,** 171403 (2023).

[193] gwosc.org.